Genetic validation of *Pf*FKBP35 as an antimalarial drug target

Basil T. Thommen[1,2], Jerzy M. Dziekan[3], Fiona Achcar[4,5], Seth Tjia[3], Armin Passecker[1,2], Katarzyna Buczak[2], Christin Gumpp[1,2], Alexander Schmidt[2], Matthias Rottmann[1,2], Christof Grüring[1,2], Matthias Marti[4,5], Zbynek Bozdech[3], Nicolas M. B. Brancucci[1,2]

[1]Department of Medical Parasitology and Infection Biology, Swiss Tropical and Public Health Institute, 4123 Allschwil, Switzerland.

[2]University of Basel, 4001 Basel, Switzerland.

[3]School of Biological Sciences, Nanyang Technological University, Singapore.

[4]Wellcome Center for Integrative Parasitology, Institute of Infection, Immunity and Inflammation, University of Glasgow, Glasgow, UK.

[5]Institute for Parasitology, VetSuisse and Medical Faculty, University of Zurich, Zurich, Switzerland.

Correspondence:
Nicolas M. B. Brancucci, nicolas.brancucci@swisstph.ch

Keywords: malaria, *Plasmodium falciparum*, ribosome homeostasis, FKBP35, FK506, CETSA, antimalarial drugs

Abstract

Plasmodium falciparum accounts for the majority of over 600'000 malaria-associated deaths annually. Parasites resistant to nearly all antimalarials have emerged and the need for drugs with alternative modes of action is thus undoubted. The FK506-binding protein *Pf*FKBP35 has gained attention as a promising drug target due to its high affinity to the macrolide compound FK506 (tacrolimus). Whilst there is considerable interest in targeting *Pf*FKBP35 with small molecules, a genetic validation of this factor as a drug target is missing and its function in parasite biology remains elusive. Here, we show that limiting *Pf*FKBP35 levels are lethal to *P. falciparum* and result in a delayed death-like phenotype that is characterized by defective ribosome homeostasis and stalled protein synthesis. Our data furthermore suggest that FK506, unlike the action of this drug in model organisms, exerts its anti-proliferative activity in a *Pf*FKBP35-independent manner and, using cellular thermal shift assays, we identify putative FK506-targets beyond *Pf*FKBP35. In addition to revealing first insights into the function of *Pf*FKBP35, our results show that FKBP-binding drugs can adopt non-canonical modes of action – with major implications for the development of FK506-derived molecules active against *Plasmodium* parasites and other eukaryotic pathogens.

37 # 1 Introduction

38 Despite considerable progress in recent years, malaria remains one of the major global health
39 threats (1). The apicomplexan parasite *Plasmodium falciparum* is responsible for the vast
40 majority of the over 600'000 malaria deaths in 2020. Most of this burden is carried by infants
41 and children under the age of five in sub-Saharan Africa. Malaria deaths increased by 12%
42 compared to 2019, which can at least in part be explained by the COVID-19 related suspension
43 of malaria control and treatment measures (1). In addition, the emergence of parasites resistant
44 to most antimalarials, including artemisinin-based combination therapies, endangers current
45 and future disease elimination efforts and underscores the need for developing drugs with
46 alternative modes of action (2).

47 FK506 (tacrolimus), a well-characterized immunosuppressant, shows considerable activity
48 against asexual blood stage parasites (3). *P. falciparum* encodes a single FK506-binding protein
49 (FKBP) dubbed *Pf*FKBP35 (PF3D7_1247400), which is considered to be a promising drug
50 target (4, 5). FKBPs belong to the immunophilin family and are conserved throughout the
51 eukaryotic kingdom (6, 7). In contrast to the malaria parasite, most other eukaryotes encode
52 several FKBPs that, besides showing high affinity for the FK506 drug, exert peptidyl-prolyl
53 isomerase (PPIase) activity. The PPIase moiety catalyzes cis-trans isomerization of proline
54 residues – an event thought to be rate-limiting for the folding of many proteins (8). Independent
55 of their PPIase activity, FKBPs act as chaperones to prevent protein aggregation under stress
56 conditions (9, 10). Furthermore, some FKBP variants play a role in cellular signaling or gene
57 regulation (11, 12). Human FKBP12 for instance is best-known for its ability to form a complex
58 with the immunosuppressant drugs FK506 and rapamycin. These complexes inhibit the
59 phosphatase activity of calcineurin and the kinase activity of mTOR (mechanistic target of
60 rapamycin), respectively (13). Amongst many other effects, this inhibition results in decreased
61 T-cell activation. Of note, the regulatory role of *Hs*FKBP12 depends on the presence of
62 rapamycin or FK506. In absence of drugs, this immunophilin neither interacts with mTOR nor
63 with calcineurin and does hence not affect activity of these key components of eukaryotic cells.
64 Due to the conserved nature of FKBPs, rapamycin and FK506 have also gained attention as
65 potential antimicrobial drugs (3, 7).

66 Similar to its homologs in model organisms, *Pf*FKBP35 harbors PPIase and chaperoning
67 activity *in vitro* (5). Despite sharing key features with FKBPs of other eukaryotes, its role in *P.*
68 *falciparum* remains elusive. *Pf*FKBP35 is believed to interact with heat shock proteins (HSPs)
69 and co-immunoprecipitates with cytoskeletal factors of *P. falciparum* (14). While *Pf*FKBP35

is inhibiting the phosphatase activity of recombinant calcineurin in a FK506-independent manner (15-17), it does not co-localize with calcineurin *in vivo* (16). The protein is expressed throughout the 48-hour intra-erythrocytic development of *P. falciparum* and is found within the cytosol of ring stage parasites. In the older trophozoite and the replicating schizont stages, the protein was reported to also localize to the nucleus (16). While a transposon-based mutagenesis screen suggests that *Pf*FKBP35 is essential for intra-erythrocytic replication (18), neither its cellular function nor its essentiality was confirmed experimentally in live parasites. The unknown role in parasite biology notwithstanding, *Pf*FKBP35 is considered to be a viable drug target and, given the fact that *P. vivax* and *P. knowlesi* encode FKBP homologs that exhibit comparable PPIase activities (19, 20), future FKBP-targeted therapies may be effective across different *Plasmodium* species.

Crystal structures of *Pf*FKBP35 in complex with FK506 and rapamycin revealed high affinity interactions with the FK506-binding domain of the protein (15, 21, 22). Consistent with these observations, *in vitro* enzyme activity assays showed that FK506 inhibits the PPIase activity of recombinant *Pf*FKBP35 in a dose-dependent manner (5). Previous research aimed at exploiting structural differences between human and parasite-encoded FKBPs to circumvent the immunosuppressive activity of drug-bound *Hs*FKBP12 (23-26). These efforts include investigation of non-covalent FKBP inhibitors such as adamantyl derivatives, macrocycles, the small molecule D44 (23-25, 27, 28) and the synthetic ligand for FKBP (SLF) as well as derivatives thereof designed to covalently bind *Pf*FKBP35 (29). While D44 shows promising antimalarial activity, it fails to alter thermostability of the FK506-binding domains of *Pf*FKBP35 and *Hs*FKBP12 *in vitro* (29), suggesting that this compound does not directly interact with *Pf*FKBP35. Up until now, *Pf*FKBP35 has not been validated as a drug target using reverse genetics, and the link between *Pf*FKBP35-interacting drugs and their antimalarial activity remains elusive (3).

Here, we generated inducible *Pf*FKBP35 knock-out, knock-down as well as over-expression cell lines and demonstrate that *Pf*FKBP35 is essential for asexual replication of blood forms. We show that the knock-out of *Pf*FKBP35 results in reduced levels of ribosomal proteins and stalled protein synthesis. However, these effects are not reflected in the parasite transcriptome, indicating a vital role at the post-transcriptional level. While the mechanistic link between *Pf*FKBP35 and ribosome homeostasis remains elusive, our data underpins the potential of *Pf*FKBP35 as a drug target and, using cellular thermal shift assays (CETSA), we corroborate the high affinity binding of FK506 to *Pf*FKBP35. Importantly, however, our data does not

support scenarios in which FK506 inhibits the essential function of *Pf*FKBP35, suggesting that it exerts its antimalarial activity in a *Pf*FKBP35-independent manner, which has major implications for the development of future FK506-based antimalarials and/or *Pf*FKBP35-inhibiting drugs.

2 Results

2.1 *Pf*FKBP35 is essential for asexual replication

In a first step, using CRISPR/Cas9-mediated gene editing, we engineered a *P. falciparum* cell line allowing for a conditional knock-down of *Pf*FKBP35 using the DD/Shield system (30, 31) (Figs. 1A and S1A-B). Despite the efficient depletion of *Pf*FKBP35 under knock-down conditions, parasites did not show apparent growth defects (Figs. S1C-D). Immunofluorescence assays (IFA) showed that *Pf*FKBP35 localizes to distinct foci within the parasite nucleus (Fig. 1B).

Next, we generated a cell line allowing for the conditional knock-out of the endogenous coding sequence using a dimerizable Cre recombinase (DiCre)-based system (32). Specifically, we introduced two *loxP* sites – one within a synthetic intron (33) downstream of the start codon and one after the stop codon of the *fkbp35* coding region – and added a *green fluorescent protein* (*gfp*) sequence downstream of this expression cassette (Figs. 1C, S2A). As a result, these NF54/iKO-FKBP35 parasites express tag-free, wild-type (WT) *Pf*FKBP35 protein under control conditions (FKBP35$^{\mathbf{WT}}$). Upon DiCre activation, the *loxP* sites are recombined and the *fkbp35* locus is excised from the parasite genome (Figs. 1C, S2B). Under these knock-out conditions (FKBP35$^{\mathbf{KO}}$), parasites express cytosolic GFP under control of the endogenous *fkbp35* promoter. This setup allows monitoring knock-out efficiency at the single cell level and revealed that DiCre successfully deleted *fkbp35* in the vast majority of parasites (Fig. 1D).

In a first attempt, we induced the *fkbp35* knock-out in synchronous ring stage NF54/iKO-FKBP35 parasites at 0-6 hours post erythrocyte invasion (hpi), i.e. prior to the expected peak transcription of *fkbp35* (34). These FKBP35$^{\mathbf{KO}}$ parasites showed a delayed death-like phenotype. In the first generation (G1), parasites completed intra-erythrocytic development without noticeable effects (Fig. 1E) and entered the next generation (G2) with a multiplication rate similar to that of the FKBP35$^{\mathbf{WT}}$ control population (Fig. 1F). In G2, however, FKBP35$^{\mathbf{KO}}$ parasites arrested at the late trophozoite/early schizont stage (approximately 30-36 hpi) with many cells failing to enter DNA replication in the S-phase (Fig. 1E). To investigate this

135 phenomenon in more detail, we induced the *fkbp35* knock-out at three different time points
136 during the IDC. Similar to DiCre activation at 0-6 hpi, knocking out *fkbp35* at 12-18 hpi resulted
137 in parasite death at the trophozoite/schizont stage of the subsequent generation. However, when
138 induced at 24-30 hpi or 34-40 hpi in G1, parasites did not only complete the current IDC but
139 also successfully passed through G2 before they eventually arrested in G3 (Fig. 1G).
140 Considering that low *Pf*FKBP35 levels are sufficient to maintain the essential function of the
141 protein, as observed with the NF54/iKD-FKBP35 parasites (see Fig. S1C-D), it is conceivable
142 that proteins expressed between 0 and 24hpi, i.e. prior to deleting *fkbp35* from the genome,
143 allow parasites to enter G3.

144 The delayed death of FKBP35^{KO} is reminiscent of a phenotype observed in apicoplast-deficient
145 parasites (35, 36). We therefore tested if *Pf*FKBP35 is involved in apicoplast biology, i.e. the
146 synthesis and/or export of isoprenoid precursors, but did not find evidence for an association
147 with this organelle (Fig. S2C). Furthermore, given the reported interaction of *Pf*FKBP35 with
148 heat shock proteins (14, 16), we also tested the parasite`s response to heat stress, but could not
149 detect altered heat-susceptibility between FKBP35^{KO} and FKBP35^{WT} cells (Fig. S2D).

150

151 ## 2.2 *Pf*FKBP35 is crucial for ribosome homeostasis and protein synthesis

152 To further elucidate the function of *Pf*FKBP35, we induced the *fkbp35* knock-out in early ring
153 stages (0-6 hpi) and compared the proteomes of FKBP35^{KO} and FKBP35^{WT} parasites at the
154 schizont stage of G1 (36-42 hpi) and at the trophozoite stage of the following generation (G2,
155 24-30 hpi) using a quantitative proteomics approach.

156 ### 2.2.1 The knock-out of *Pf*FKBP35 causes accumulation of pre-ribosome components in G1

157 Consistent with the efficient deletion of *fkbp35* on the genomic level, FKBP35^{KO} schizonts of
158 G1 showed a 19-fold (18.9 +/-5.7 s.d.) reduction of FKBP35 and GFP levels were increased by
159 84-fold (83.7 +/-38.5 s.d.) when compared to the control population (Fig. 2A, Table S1).
160 Besides *Pf*FKBP35 and GFP, 50 parasite proteins were significantly deregulated in FKBP35^{KO}
161 schizonts and 34 of them found at elevated levels compared to the FKBP35^{WT} control
162 conditions. A gene ontology analysis using PANTHER (37) indicated enrichment of the "*pre-*
163 *ribosome*" (fold enrichment = 30.4, p-value = 1.46E-5, 4/34 proteins) and "*nucleolus*" (fold
164 enrichment = 6.77, p-value = 8.85E-4, 5/34 proteins) terms among these factors. While the pre-
165 ribosome is a large subunit precursor of mature ribosomes, the nucleolus represents the primary
166 site for the biogenesis of ribosomal subunits (38). In contrast to factors being more abundant in

167 knock-out parasites, none of the 16 factors with lower abundance in FKBP35^{KO} cells were
168 associated with ribosome-related processes (Table S1). Despite being phenotypically silent in
169 G1, the accumulation of pre-ribosome and nucleolar components hints at perturbed ribosome
170 maturation in these cells. Specifically, it is conceivable that the observed buildup of ribosome
171 intermediates results from reduced anabolic activity, i.e. the stalling of nucleolar pre-ribosome
172 assembly (39).

173 Notwithstanding these effects, FKBP35^{KO} cells were equally sensitive to the translation
174 inhibitor cycloheximide compared to their FKBP35^{WT} counterparts (Fig. 2B), indicating that
175 ribosome function is not compromised at this point in time (40). This is consistent with normal
176 cell cycle progression in G1 and unaltered multiplication rates of FKBP35^{KO} parasites, as
177 described above (see Figs. 1E-F), and shows that the prominent depletion of *Pf*FKBP35 does
178 not have a major impact on parasite viability in G1.

179 **2.2.2 *Pf*FKBP35 is essential for maintaining normal levels of functional ribosomes in G2**

180 In the following generation (G2, 24-30 hpi), the proteome of FKBP35^{KO} trophozoites showed
181 substantial differences. Despite the absence of morphological changes at this point in time, 216
182 proteins were significantly deregulated (Fig. 2C). Among these, 50 proteins were found at
183 higher abundance compared to FKBP35^{WT} and their gene ontology terms point towards an
184 effect on processes involved in energy metabolism (Fig. 2D).

185 The majority of deregulated factors (166 of 216) in G2, however, were less abundant in
186 FKBP35^{KO} compared to the FKBP35^{WT} control cells. Very prominently, 20 of the top 50 hit
187 molecules are ribosomal proteins that, on average, show a two-fold reduction (2.0 +/- 0.4 s.d.)
188 in FKBP35^{KO} parasites (Table S1). It is therefore not surprising that PANTHER identified the
189 knock-out of *Pf*FKBP35 to mainly affect ribosome-related processes, such as "*cytoplasmic*
190 *translation*", "*ribosome assembly*", and "*ribosomal large subunit biogenesis*" (Fig. 2D) (37).

191 To assess if the reduced levels of ribosomal proteins result in lower protein synthesis rates, we
192 employed the "surface sensing of translation" (SUnSET) technique. SUnSET is based on
193 incorporation of the tyrosyl-tRNA analogue puromycin into nascent peptide chains and thereby
194 allows monitoring newly synthesized proteins (41). As expected, we found that FKBP35^{KO}
195 trophozoites in G2 (24-30 hpi) showed reduced translation rates compared to the FKBP35^{WT}
196 control population (Fig. 2E), while protein synthesis was not affected under control conditions
197 (rapamycin-induced DiCre activation in the NF54/DiCre parental line (Fig. S2E)).

198 Taken together, these results indicate that, under knock-out conditions, *Pf*FKBP35 levels
199 become limiting for ribosome maturation late during schizogony of G1, without having
200 immediate effects on the steady-state levels of mature ribosomes. The knock-out of *Pf*FKBP35
201 is thus phenotypically silent in G1. In absence of a continuous supply of mature ribosomes
202 under FKBP35^{KO} conditions, however, FKBP35^{KO} parasites fail at maintaining translation at a
203 level that would support normal parasite development in the next generation (G2).

204

205 **2.3 The knock-out of *Pf*FKBP35 is transcriptionally silent**

206 To examine if the altered proteome of FKBP35^{KO} parasites is the result of *Pf*FKBP35-
207 controlled transcription, we compared the transcriptional profiles of FKBP35^{WT} and
208 FKBP35^{KO} in a time course RNA-Sequencing (RNA-Seq) experiment spanning two IDCs.
209 Specifically, we induced the knock-out of FKBP35 in synchronous parasites at 0-6 hpi and
210 collected RNA from parasite populations at three and four subsequent time points (TPs) in G1
211 and G2, respectively (Figs. 3A, S3A). With the exception of TP7, these time points cover a time
212 frame during which FKBP35^{KO} cells cannot be distinguished from their FKBP35-expressing
213 counterparts on a morphological level (compare Fig. 1E).

214 As expected, the transcriptome of FKBP35^{KO} showed a prominent reduction of steady-state
215 *fkbp35* transcripts already in TP1 (11.3-fold +/-2.0 s.d.) compared to the FKBP35^{WT} control
216 population (Fig. S3B, Table S2). During peak transcription at 30-36 hpi (TP2), this difference
217 increased to 240-fold (238.4 +/-20.0 s.d.) and, consistent with the efficient recombination at the
218 *fkbp35* locus, these cells started transcribing *gfp*. Notwithstanding the prominent depletion of
219 *fkbp35* transcripts, the transcriptome of FKBP35^{KO} is only marginally affected up to and
220 including 24-30 hpi in G2 (TP6). By contrast, at 30-36 hpi (TP7) the transcription of knock-out
221 parasites shows major changes (Fig. 3B). Considering the appearance of morphological changes
222 in FKBP35^{KO} at this time point, effects on the transcriptome are unlikely to represent specific
223 activities of *Pf*FKBP35 in gene regulation. Indeed, mapping the transcriptome of individual
224 time points to a high resolution reference (42), revealed a significant slow-down of FKBP35^{KO}
225 compared to FKBP35^{WT} parasites at TP7 (Figs. 3C, S3C). This indicates aborted cell cycle
226 progression in FKBP35^{KO} parasites during a phase that is characterized by a rapid increase in
227 biomass – possibly due to a translation and/or size-dependent cell cycle checkpoint (43). At
228 earlier time points (TP1-TP6), the transcriptomes of FKBP35^{KO} and FKBP35^{WT} are highly
229 comparable and the differences observed on the level of individual genes clearly fail at

230 explaining the proteomic changes observed in FKBP35^{KO} parasites at 24-30 hpi in G2 (TP6),
231 reiterating that the essential activity of *Pf*FKBP35 is linked to transcription-independent
232 processes.

233

234 **2.4 Probing FK506 interactions in Cellular Thermal Shift Assays (CETSA)**

235 *Pf*FKBP35 emerged as a promising antimalarial drug target (4) and considerable efforts were
236 made to define interactions of this immunophilin with small molecules in the last decade (24-
237 26, 44). Several studies conclusively demonstrated that FK506 – the most well-known ligand
238 of mammalian FKBPs (45) – binds to *Pf*FKBP35 (15, 21, 22) and kills asexual blood stage
239 parasites with a half-maximal inhibitory concentration (IC50) in the low micromolar range at
240 1.9 µM (3).

241 To investigate interactions of FK506 with *P. falciparum* proteins, we used the *cellular thermal*
242 *shift assay followed by mass spectrometry* (MS-CETSA). This approach exploits the fact that,
243 once drug-protein complexes are formed, thermostability of the target protein is altered (46).
244 We applied the so-called *isothermal dose-response* variant of CETSA using FK506 (47). Here,
245 target proteins are identified based on their dose-dependent stabilization by drugs under thermal
246 challenge (different temperatures) when compared to a non-denaturing condition (37 °C), using
247 the change in the area under the curve (ΔAUC) and the dose-response curve goodness of fit
248 (R^2) as metrics (Fig. 4A) (47).

249 **2.4.1 CETSA identifies targets of FK506**

250 In a first step, we performed CETSA in combination with drug-exposed protein extracts. Since
251 proteins lose their physiological context during the process of protein extraction, this variant of
252 the CETSA approach is designed to identify direct protein-drug interactions (46, 47). Not
253 surprisingly, we found *Pf*FKBP35 to be stabilized by FK506 in a dose-dependent manner when
254 challenged at 60 °C with a half maximal effective concentration (EC50) of 152.0 nM (Fig. 4B).
255 The fact that FK506 exhibits its stabilizing activity already in the low nanomolar concentration
256 range indicates high affinity interactions between the protein-drug pair.

257 Besides *Pf*FKBP35, FK506 stabilizes a number of other proteins in a dose-dependent manner
258 (Figs. 4C and S6). A few of these factors show pronounced sigmoidal stabilization profiles and
259 are predicted to be essential (Fig. 4C) (18). Amongst others, N6-methyl transferase MT-A70
260 (PF3D7_0729500), histone deacetylase HDA2 (PF3D7_1008000), pre-mRNA-splicing factor

261 CEF1 (PF3D7_1033600), FeS cluster assembly protein SufD (PF3D7_1103400) and the
262 H/ACA ribonucleoprotein complex subunit 1 (PF3D7_1309500) showed most pronounced
263 stabilization profiles (Fig. S6 and Table S3). In contrast to *Pf*FKBP35, most of these likely
264 essential candidates are stabilized at FK506 concentrations close to the drug`s IC50 (3). It can
265 therefore not be excluded that the binding of FK506 to at least one of these factors is contributes
266 to the antimalarial activity of the drug.

267 **2.4.2 The *Pf*FKBP35/FK506 pair interferes with ribosomal complexes**

268 Given the high-affinity interaction of *Pf*FKBP35 with FK506 and its association with ribosomal
269 proteins, we set out to describe the native context of *Pf*FKBP35 using the "live cell variant" of
270 CETSA. In contrast to focusing exclusively on direct protein-drug interactions, live cell CETSA
271 allows capturing drug-induced shifts in protein stability beyond those of direct binding partners
272 (47) and amongst others allows identifying factors present in the same protein complex as the
273 target protein. To do so, CETSA takes advantage of the fact that factors within complexes have
274 similar denaturation temperatures due to their co-aggregation upon heat-induced denaturation
275 (48). As a consequence, this CETSA variant generally identifies more factors compared to the
276 protein extract-based CETSA approach (Fig. 4A).

277 As expected, and confirming the results above, live cell CETSA shows that FK506 alters the
278 thermal stability of *Pf*FKBP35 already at very low drug concentrations when challenged at 60
279 °C with an EC50 of 286.7 nM (Fig. 4B). Interestingly, and in contrast to the protein lysate-
280 based approach, live cell CETSA revealed that more than 50 ribosomal proteins are stabilized
281 in presence of FK506 when challenged at 55 °C, with a median EC50 of 45.9 nM (25th
282 percentile = 34.2, 75th percentile = 58.9). Of note, these ribosomal proteins were stabilized at
283 virtually identical FK506 concentrations (Figs. 4D, and S7), indicating that the drug – directly
284 or indirectly – interacts with ribosomal complexes. This is in further agreement with the fact
285 that these ribosomal factors were not identified by protein lysate-based CETSA (compare Figs.
286 4A, S6).

287 Worth mentioning, we observed a drug dose-dependent increase in soluble protein abundance
288 of ribosomal proteins also under non-denaturing conditions, i.e. at 37 °C, with a median EC50
289 of 1.94 µM (25th percentile = 1.85, 75th percentile = 2.1) (Figs. 4D, S7). Generally, due to the
290 absence of a denaturing heat challenge, such a drug-dependent enrichment in soluble protein
291 levels does not indicate binding-induced thermal stabilization of proteins (47). Instead, this can
292 be the result of increased protein synthesis, altered protein conformation or, alternatively, occur

293 in response to factors disengaging from larger protein complexes. The fact that FK506
294 solubilizes a high number of ribosomal proteins within a very narrow concentration window
295 also at 37 °C, implies that these factors are liberated from the same ribosomal complex or from
296 complexes that interact with each other and shows that FK506 negatively affects stability of
297 ribosomal structures in live cells. However, these effects are limited to high, presumably
298 saturating FK506 concentrations. Importantly, the vast majority of ribosomal proteins identified
299 in live cell CETSA are shared with those de-regulated in *Pf*FKBP35 knock out cells (Fig. 4E),
300 pointing towards a shared localization of FK506 and its *Pf*FKBP35 target in live parasites.

301 Together with the above-described importance of *Pf*FKBP35 in ribosome homeostasis, these
302 results strongly suggest that FK506 is recruited to the activity site of *Pf*FKBP35 – most
303 probably the nucleolar maturation sites of ribosomes – where it interacts with ribosomal
304 complexes.

305

306 **2.5 FKBP-targeting drugs act in an *Pf*FKBP35-independent manner**

307 Considering the proposed direct interaction between FK506 and FKBP35 in *P. falciparum*, we
308 expected that FKBP35^{KO} parasites show altered sensitivity to the drug. Consistent with
309 published data, FK506 killed FKBP35^{WT} cells with an IC50 of 1942 nM (+/-193 nM s.d.) when
310 administered at 4-10 hpi in G1 (Fig. 4F). Surprisingly however, and despite the prominent
311 depletion of the protein under knock-out conditions, FKBP35^{KO} and FKBP35^{WT} parasites were
312 equally sensitive to FK506 (IC50 = 1741 nM +/- 187 s.d.) (Fig. 4F). Similarly, neither the
313 efficient knock-down of *Pf*FKBP35 in NF54/iKD-FKBP35 parasites (compare Fig. S1C), nor
314 its over-expression (OE) in NF54/iOE-FKBP35 cells (Fig. S4A-C), resulted in the expected
315 sensitivity change to FK506 treatment (Fig. 4G). In addition to this apparent independence of
316 the drug to varying *Pf*FKBP35 levels, and in agreement with earlier studies (3, 24, 49), FK506
317 unfolds its antimalarial activity within the same cycle after treatment. This immediate activity
318 of the drug stands in stark contrast to the delayed death-like phenotype of FKBP35^{KO} parasites
319 (compare Fig. 1E-G), substantiating the notion that FK506 must target essential parasite factors
320 other than *Pf*FKBP35.

321 To rule out that the timing of drug exposure is masking expected links between FK506 and
322 *Pf*FKBP35, we tested whether administering FK506 at 30-36 hpi and 36-42 hpi (instead of 4-
323 10 hpi) affects parasite survival in a *Pf*FKBP35-dependent manner (Figs. 4F and S5A).
324 However, we did not observe a change in FK506 susceptibility compared to FKBP35^{WT}

325 parasites, ruling out the possibility that FKBP35^{KO} parasites were killed by FK506 before
326 *Pf*FKBP35 levels were different in the two populations. Further, to account for a scenario in
327 which the activity of FK506 on *Pf*FKBP35 is masked by a temporal delay between drug
328 exposure and parasite killing, we induced the knock-out of *Pf*FKBP35 at 34-40 hpi (instead of
329 0-6 hpi) and allowed FKBP35^{KO} parasites to proceed to G2, before exposing them to different
330 FK506 concentrations. Despite these efforts, FKBP35^{WT} and FKBP35^{KO} parasites were equally
331 sensitive to FK506 (Fig. S5B, S5C) and the calcineurin inhibitor cyclosporin A (Fig. S5D-E).

332 In addition to FK506, we evaluated the *Pf*FKBP35-specific inhibitor D44 (N-(2-Ethylphenyl)-
333 2-(3h-Imidazo[4,5-B]pyridin-2-Ylsulfanyl)acetamide) but, surprisingly, we failed to reproduce
334 the previously reported dose-response effect (24). We tested D44 from two suppliers using
335 NF54/iKO-FKBP35, NF54 wild type and K1 parasite strains using different assay setups,
336 including the gold standard method that is based on the incorporation of tritium labeled
337 hypoxanthine into DNA of replicating cells (50). Still, we could not detect any activity of D44
338 on asexual replication of blood stage parasites (Figs. S5F-G).

339 Taken together, these results are in clear conflict with the perception that FK506 and D44 kill
340 parasites by targeting *Pf*FKBP35 exclusively.

341

342 # 3 Discussion

343 Members of the FKBP family are involved in regulating diverse cellular processes in eukaryotic
344 as well as in prokaryotic cells (8, 51). In contrast to most other eukaryotes, the human malaria
345 parasite *P. falciparum* encodes a single FKBP only (16). The enzymatic activity of *Pf*FKBP35,
346 as well as the interactions of the protein with FKBP-targeting drugs, was subject to considerable
347 drug-focused research *in vitro*. Besides demonstrating the drug`s affinity to *Pf*FKBP35 by co-
348 crystallization, these efforts uncovered that FK506 inhibits enzymatic activity of the protein`s
349 PPIase domain (5). Together with the anti-malarial activity of FK506, these data offered
350 compelling evidence for an essential but yet uncharacterized role of *Pf*FKBP35 during blood
351 stage development of *P. falciparum*.

352 Here, we set out to investigate the role of *Pf*FKBP35 in parasite biology. Using an inducible
353 knock-out approach, we show that *Pf*FKBP35 is indeed essential for intra-erythrocytic
354 development of asexually replicating *P. falciparum* parasites and CETSA experiments
355 confirmed high affinity binding of FK506 to its *Pf*FKBP35 target. While the knock-out of
356 *Pf*FKBP35 does not markedly affect transcription, FKBP35^{KO} cells show reduced levels of

357 ribosomal proteins and impaired protein synthesis on the global scale. Surprisingly however,
358 these effects, as well as the consequent death during the late trophozoite/early schizont stage,
359 only manifest in the cycle following knock-out induction without affecting cell cycle
360 progression in the first generation (G1) or multiplication rates from G1 to G2. In contrast to the
361 delayed death-like phenotype of FKBP35^{KO} cells, FK506 unfolds its parasiticidal activity
362 without a lag phase, i.e. within the IDC of treatment (24), and the dose-response relationship
363 between FK506 and parasite death is irresponsive to altered *Pf*FKBP35 levels. Taken together,
364 our data strongly indicate that the parasite-killing activity of FK506 is *Pf*FKBP35-independent.

365 Knocking out *Pf*FKBP35 early during intra-erythrocytic development has only minor effects
366 on the parasite proteome in G1. Being relatively subtle, these changes may still point towards
367 an important function of *Pf*FKBP35: Factors associated with the nucleolus – the site of
368 ribosome biogenesis – are found at higher abundance in knock-out cells. In the next cycle,
369 FKBP35^{KO} parasites show a dramatic decrease of factors associated with ribosome- and
370 translation-related processes and, likely a consequence thereof, globally reduced protein
371 synthesis during trophozoite development (G2, 24-30 hpi). Importantly, at this point in time,
372 FKBP35^{KO} cells still show ordinary morphology and their transcriptional activity remains
373 largely unaffected. The observed changes in the abundance of ribosomal factors must therefore
374 result from transcription-independent activity of *Pf*FKBP35. While ribosomal components are
375 present at higher levels in G1, they are drastically reduced in FKBP35^{KO} cells in G2. These
376 opposing effects likely result from *Pf*FKBP35 activity in a shared cellular process. Specifically,
377 it is conceivable that low *Pf*FKBP35 levels inhibit ribosome maturation in G1, explaining the
378 accumulation of (pre-) ribosomal factors. While the levels of functional ribosomes are sufficient
379 to support continued translation in G1, ribosomes likely become limiting in the next generation
380 (G2), which eventually results in stalled translation activity and concomitant parasite death at
381 the onset of schizogony.

382 In contrast to the significant effects on the protein levels in G2, the transcription of FKBP35^{KO}
383 remains largely unaffected by the loss of *Pf*FKBP35 and becomes apparent only during late
384 trophozoite/early schizont development in G2 (30-36 hpi); i.e. at a time during which cell cycle
385 progression is slowed down in FKBP35^{KO} parasites. In fact, at this stage the transcriptional
386 signature of FKBP35^{KO} parasites is dominated by the slowed progression through intra-
387 erythrocytic development, rather than resulting from specific gene regulatory events. While this
388 stalling is consistent with the observed effects on ribosome homeostasis and protein synthesis,

389 it demonstrates that, in contrast to certain FKBP family members in other organisms,
390 *Pf*FKBP35 does not have apparent roles in transcriptional control.

391 Regarding the well-characterized and fast-acting parasiticidal activity of FK506 on *P.*
392 *falciparum*, it was somewhat surprising to observe a delayed death-like phenotype for
393 *Pf*FKBP35 knock-out parasites (24). We hence set out to investigate unifying explanations. The
394 delayed death of FKBP35^{KO} parasites is most easily be explained by residual activity of
395 *Pf*FKBP35 proteins synthesized prior to inducing the genomic knock-out of *fkbp35*. In such a
396 scenario, low *Pf*FKBP35 in FKBP35^{KO} would be sufficient to allow completion of the IDC,
397 before eventually dropping below a level that is required for supporting parasite survival in the
398 next cycle. Despite intense efforts, we failed at confirming this hypothesis and our data strongly
399 favors an alternative scenario in which FK506 kills parasites in a *Pf*FKBP35-idenpendent
400 manner. Aside from the fact that FK506 exerts its parasiticidal activity within the same IDC,
401 neither the conditional knock-out, knock-down nor the overexpression of *Pf*FKBP35 altered
402 the parasite's sensitivity to FK506; and this irrespective of the profoundly deregulated
403 *Pf*FKBP35 levels in the respective mutant lines (Fig. 4F). For instance, administering FK506
404 36 hours post induction of the knock-out in early ring stages (36-42 hpi) – i.e. at a time point
405 where FKBP35^{KO} cells are only left with about 5% of the regular *Pf*FKBP35 levels (19-fold
406 reduction compared to FKBP35^{WT} parasites, Fig. 2A) – does not affect the dose-response of
407 parasites to the drug. Further, our attempts to demonstrate that the timing of drug exposure is
408 masking the expected links between FK506 and its *Pf*FKBP35 drug target failed (compare Figs.
409 4A and S5A-C). Our data is thus incompatible with the notion that the parasite-killing activity
410 of FK506 results from inhibiting the essential function of *Pf*FKBP35.

411 Since binding of FK506 to *Pf*FKBP35 alone cannot explain the drug's antimalarial activity, we
412 aimed identifying additional FK506 targets. CETSA performed on protein lysates identified a
413 number of parasite factors binding to FK506. Compared to the *Pf*FKBP35/FK506 pair,
414 however, these interactions are of considerably lower affinity. The adenosine-methyltransferase
415 MT-A70 (PF3D7_0729500) and the pre-mRNA-splicing factor CEF1 (PF3D7_1033600), for
416 instance, were stabilized by FK506 with EC50 concentrations of 2.0 and 3.1 µM, respectively.
417 While this affinity is relatively poor compared to the strong interaction formed between
418 *Pf*FKBP35 and FK506, one should be cautious designating the binding of FK506 to these
419 proteins as irrelevant "*off-target*" effects. In fact, their inhibition may hypothetically mask
420 effects of FK506 on *Pf*FKBP35 – a possibility that shall briefly be discussed in the following
421 section.

422 Assuming that FK506 is inhibiting the essential function of *Pf*FKBP35, one would expect
423 parasites to show a delayed death-like phenotype similar to that observed in FKBP35^{KO}
424 parasites. The presence and inhibition of other essential targets may, however, mask such an
425 effect. Consistent with this possibility, FK506 kills *P. falciparum* parasites at 1.9 µM (+/-0.2
426 µM s.d.), i.e. at concentrations similar to those required for stabilizing MT-A70 and CEF1 under
427 thermal challenge in CETSA. However, numerous attempts to prove that FK506 indeed inhibits
428 essential *Pf*FKBP35 functions failed: Neither knocking out *Pf*FKBP35 at different time points
429 nor adding FK506 to different stages of FKBP35^{KO} parasites could provide evidence for a
430 *Pf*FKBP35-dependent effect. This indicates that either the binding of FK506 does not interfere
431 with the essential role of *Pf*FKBP35, or that *Pf*FKBP35 is inhibited only at high FK506
432 concentrations that also inhibit other essential factors. In this context it is worth mentioning that
433 parasites remain unaffected by a highly efficient knock-down of endogenous *Pf*FKBP35
434 (observed with NF54/iKD-FKBP35; compare Figs. S1C-D), which demonstrates that very low
435 protein levels are sufficient to maintain the essential function of *Pf*FKBP35. It is thus
436 conceivable that high FK506 concentrations are required to fully inhibit *Pf*FKBP35 – a view
437 that is further supported by data obtained with the live cell CETSA approach discussed
438 hereafter.

439 Besides identifying direct binding of drugs to their target, live cell CETSA allows capturing
440 indirect effects on factors that act in the same pathway or in the same protein complex as the
441 drug-bound target (47). While this approach confirmed the high affinity binding of FK506 to
442 *Pf*FKBP35, it also revealed that more than 50 ribosomal proteins share a very prominent
443 CETSA signature: First, they are thermally stabilized by FK506 within a narrow concentration
444 window of the drug. Second, higher levels of FK506 increase the solubility of these ribosomal
445 components also at 37 °C. These results indicate that the FK506/*Pf*FKBP35 pair interacts with
446 ribosomal complexes and that FK506 is able to induce the dissociation of these ribosomal
447 structures under physiological conditions. Importantly, and in contrast to the binding of FK506
448 to *Pf*FKBP35, this effect on ribosomes is only observed at high concentrations of the drug.
449 Together, these data likely explain the discrepancy observed between the high binding affinity
450 of FK506 for *Pf*FKBP35 and the low or even absent effect of the drug on *Pf*FKBP35 function
451 in blood stage parasites.

452 In line with our data, previous biochemical approaches revealed potential links between
453 *Pf*FKBP35 and ribosomes. Using co-immunoprecipitation, Leneghan and colleagues revealed
454 that *Pf*FKBP35 is interacting with 480 proteins, of which 31 are ribosomal factors (14). Indeed,

455 FKBP family members are essentially involved in controlling ribosomes in other systems. The
456 human FKBP variant *Hs*FKBP25, for instance, is recruited to the pre-ribosome where its
457 chaperone activity appears to be required for the assembly of the ribosomal large subunit (52).
458 While the FKBP variant of yeast, Fpr4, interacts with the ribosome biogenesis factor Nop53
459 (53), the *Escherichia coli* trigger factor (TF) is part of the ribosomal complex and crucial for
460 the folding of nascent proteins (54, 55). Considering the marked reduction of ribosomal proteins
461 in FKBP35$^{\mathbf{KO}}$ parasites, it is tempting to speculate that *Pf*FKBP35 is chaperoning ribosome
462 biogenesis similar to Fpr4 and FKBP25 in *Saccharomyces cerevisiae* and *humans*, respectively.

463 The fact that *Pf*FKBP35 localizes to distinct nuclear foci and its depletion causes dysregulation
464 of ribosomes points towards a role within the nucleolus – the nuclear compartment driving
465 ribosome biogenesis (38). Using IFAs, we found that *Pf*FKBP35 does not co-localize with the
466 nucleolar marker fibrillarin (56) (Fig. S8). However, its localization appears to be intertwined
467 with that of this rRNA methyltransferase. Specifically, *Pf*FKBP35 is mostly found in close
468 vicinity to fibrillarin-rich regions. Nucleoli in eukaryotic cells generally consist of two or, in
469 higher eukaryotes, three sub-compartments. Of those, the granular component (GC) represents
470 the site of pre-ribosome assembly and encompasses fibrillarin-enriched central regions of
471 nucleoli (57). The spatial correlation observed between *Pf*FKBP35 and fibrillarin may thus
472 indicate localization to different sub-nucleolar compartments, with *Pf*FKBP35 occupying the
473 GC area of the nucleolus.

474 In summary, we demonstrate that limiting *Pf*FKBP35 levels are lethal to *P. falciparum* and
475 result in a delayed death-like phenotype that is characterized by perturbed ribosome
476 homeostasis and defective protein synthesis, which is likely linked to the reduced biogenesis of
477 functional ribosomes in the nucleolus. We further found no evidence that FKBP-binding drugs,
478 including FK506, exert their parasiticidal activity in a *Pf*FKBP35-dependent manner, urging
479 strong caution for the future development of FKBP-targeting antimalarials, especially when
480 based on FK506 and structural derivatives thereof. In addition to revealing first insights into
481 the essential function of *Pf*FKBP35 in ribosome homeostasis of *P. falciparum*, we are
482 convinced that the presented data offer valuable information for target-based efforts in malaria
483 drug discovery.

484

485 # 4 Methods

486 ## 4.1 Parasite culture

487 *P. falciparum* culture and synchronization was performed as described (58, 59). Parasites were
488 cultured in AB+ or B+ human red blood cells (Blood Donation Center, Zürich, Switzerland) at
489 a hematocrit of 5% in culture medium containing 10.44 g/L RPMI-1640, 25 mM HEPES, 100
490 µM hypoxanthine, 24 mM sodium bicarbonate, 0.5% AlbuMAX II (Gibco #11021-037), 0.1
491 g/L neomycin, and 2 mM choline chloride (Sigma #C7527). To achieve stabilization of DD-
492 tagged proteins in the cell lines NF54/iKD-FKBP35 and NF54/iOE-FKBP35, parasites were
493 cultured in presence of 625 nM Shield-1 (30, 31). To induce the DiCre-mediated recombination
494 of *loxP* sites in NF54/iKO-FKBP35 parasites, cultures were split and treated for 4 h with 100
495 nM rapamycin or the corresponding volume DMSO, which served as vehicle control, giving
496 rise to $FKBP35^{KO}$ and $FKBP35^{WT}$ populations, respectively (32). Cultures were gassed with
497 3% O_2, 4% CO_2 and 93% N_2 and incubated in an airtight incubation chamber at 37 °C.

498

499 ## 4.2 Cloning of transfection constructs

500 CRISPR/Cas9-based gene editing of the NF54 parasites was performed using a two-plasmid
501 approach as previously described (60, 61). This system is based on co-transfection of a plasmid
502 that contains the expression cassettes for the Cas9 enzyme, the single guide RNA (sgRNA) and
503 the blasticidin deaminase (BSD) resistance marker (pBF-gC), and a pD-derived donor plasmid
504 that contains the template for the homology-directed repair of the Cas9-induced DNA double
505 strand break (Fig. S2A) (61).

506 The plasmids pBF-gC_FKBP-3', pBF-gC_FKBP-5' and pBF-gC_P230p targeting the 3' or 5'
507 end of *fkbp35* (PF3D7_1247400) or the *p230p* (PF3D7_0208900) locus (62), respectively, were
508 generated by ligation of two annealed oligonucleotides (gRNA_top and gRNA_bottom) into
509 the BsaI-digested pBF-gC backbone (61) using T4 DNA ligase (New England Biolabs).

510 The donor plasmid pD_FKBP35-iKO was generated by assembling six DNA fragments in a
511 Gibson reaction (63) using (i) the plasmid backbone amplified by polymerase chain reaction
512 (PCR) from pUC19 (primers PCRa_F/PCRa_R) (61), (ii/iii) the 5' and 3' homology regions
513 amplified from genomic DNA (primers PCRb_F/PCRb_R and PCRc_F/PCRc_R,
514 respectively), (iv) the *green fluorescent protein* (*gfp*) sequence amplified from pHcamGDV1-
515 GFP-DD (primers PCRd_F/PCRd_R) (61), (v) the HRPII terminator amplified from genomic
516 DNA (primers PCRe_F/PCRe_R), and (vi) the *fkbp35* sequence containing an artificial *loxPint*

517 (33) amplified from a *P. falciparum* codon-optimized synthetic sequence (primers
518 PCRf_F/PCRf_R) ordered from Genscript.

519 The donor plasmid pD_FKBP35-iKD was generated by assembling five DNA fragments in a
520 Gibson reaction (63) using (i) the plasmid backbone amplified from pUC19 (primers
521 PCRa_F/PCRa_R) (61), (ii/iii) the 5' and 3' homology regions amplified from genomic DNA
522 (primers PCRg_F/PCRg_R and PCRh_F/PCRh_R, respectively), (iv) the *gfp* sequence
523 amplified from pHcamGDV1-GFP-DD (primers PCRi_F/PCRi_R) (61), and (v) the
524 destabilization domain (*dd*) sequence amplified from pHcamGDV1-GFP-DD (primers
525 PCRj_F/PCRj_R) (61).

526 The donor plasmid pD_FKBP35-iOE was generated by assembling three DNA fragments in a
527 Gibson reaction (63) using (i) the NheI/PstI-digested plasmid pkiwi003 (64), (ii) the *fkbp35*
528 coding sequence amplified from genomic DNA (primers PCRk_F/PCRk_R), and (iii) the *gfp-*
529 *dd* sequence amplified from pHcamGDV1-GFP-DD (primers PCRl_F/PCRl_R) (61).

530 Oligonucleotides are listed in Table S4.

531

532 **4.3 Transfection and selection of gene-edited parasites**

533 *P. falciparum* transfection using the CRISPR/Cas9 two-plasmid approach was performed as
534 described previously (61). Briefly, 50 µg of each plasmid (pBF-gC_FKBP-3' and pD_FKBP35-
535 iKO, pBF-gC_FKBP-5' and pD_FKBP35-iKD, pBF-gC_P230p and pD_FKBP35-iOE) were
536 co-transfected into an NF54::DiCre line (65), in which *ap2-g* was tagged with the fluorophore
537 mScarlet as described previously (66). Transgenic parasites were selected with 2.5 µg/mL
538 blasticidin-S-hydrochloride, which was added 24 h after transfection for 10 days. Transgenic
539 populations were usually obtained 2-3 weeks after transfection and correct editing of the
540 modified loci was confirmed by PCR on gDNA (Figs. S1B, S2B and S4B). Primer sequences
541 used for these PCRs are listed in Table S4. Clonal parasite lines were obtained by limiting
542 dilution cloning (67).

543

544 **4.4 DNA content analysis**

545 NF54/iKO-FKBP35 parasites were fixed in 4% formaldehyde/0.0075% glutaraldehyde for 30
546 min at room temperature and washed 3 times in PBS and stored at 4 °C. Samples were collected

547 from three independent biological replicates. RNA was digested by incubation with 0.1 mg/mL
548 RNAse A in PBS containing 0.1% Triton-X100 for 15 min at room temperature. Nuclei were
549 stained using 1X SYBR Green 1 DNA stain (Invitrogen S7563) for 20 min and washed three
550 times in PBS. The fixation step quenched the GFP signal detected by the flow cytometer (Fig.
551 S9). SYBR Green intensity was measured using a MACS Quant Analyzer 10 and analyzed
552 using the FlowJo_v10.6.1 software.

553

554 **4.5 Western blotting**

555 Saponin lysis of 500 µL infected red blood cells at 3-5% parasitaemia was performed by
556 incubation for 10 min on ice in 3 mL ice-cold 0.15% saponin in PBS. The parasite pellets were
557 washed two times in ice-cold PBS and resuspended in Laemmli buffer (62.5 mM Tris base, 2%
558 SDS, 10% glycerol and 5% 2-mercaptoethanol). Proteins were separated on 4-12% Bis-Tris
559 gels (Novex, Qiagen) using MOPS running buffer (Novex, Qiagen). Then proteins were
560 transferred to a nitrocellulose membrane (GE healthcare #106000169), which was blocked with
561 5% milk powder in PBS/0.1% Tween (PBS-T) for 1 h. The membrane was probed using the
562 primary antibodies mAb mouse α-GFP (1:1'000, Roche Diagnostics #11814460001), mAb
563 mouse α-*Pf*GAPDH (1:20'000) (68), or mAb mouse α-puromycin (1:5'000, Sigma MABE343)
564 diluted in blocking solution. After 2 h incubation, the membrane was washed 5 times in PBS-
565 T before it was incubated with the secondary antibody goat α-mouse IgG (H&L)-HRP
566 (1:10'000, GE healthcare #NXA931). After 1 h incubation, the membrane was washed 5 times
567 and the signal was detected using the chemiluminescent substrate SuperSignal West Pico Plus
568 (Thermo Scientific, REF 34580) and the imaging system Vilber Fusion FX7 Edge 17.10 SN.
569 Nitrocellulose membranes were stripped by incubating for 10 min in a stripping buffer (1 g/L
570 SDS, 15 g/L glycine, 1% Tween-20, pH 2.2) and washed three times in PBS-T before blocking
571 and re-probing.

572

573 **4.6 Drug dose-response experiments**

574 Dose-response relationships were assessed by exposing synchronous ring stage parasites at
575 0.5% parasitaemia and 1.25% hematocrit to 12 drug concentrations using a two-step serial
576 dilution in 96-well plates (Corning Incorporated, 96-well cell culture plate, flat bottom, REF
577 3596) in three independent biological replicates. The plates were gassed and incubated for 48
578 h at 37 °C. FK506 (MedChemExpress HY-13756), D44 (ChemBridge 7934155 and ChemDiv

579 7286-2836) and cyclosporin A (Sigma 30024) stocks of 10 mM were prepared in DMSO and
580 working solutions were prepared immediately before the experiment. To measure parasite
581 survival using flow cytometry, cultures were stained in 1X SYBR Green 1 DNA stain
582 (Invitrogen S7563) in a new 96-well plate (Corning Incorporated, 96-well cell culture plate,
583 round bottom, REF 3788) and incubated in the dark for 20 min. The samples were washed once
584 in PBS. Using a MACS Quant Analyzer 10, 50'000 events per condition were measured and
585 analyzed using the FlowJo_v10.6.1 software. Infected RBCs were identified based on SYBR
586 Green 1 DNA stain intensity. The gating strategy is shown in Fig. S9. To quantify parasite
587 survival based on hypoxanthine incorporation into DNA, compounds were dissolved in DMSO (10
588 mM), diluted in hypoxanthine-free culture medium and titrated in duplicates over a 64-fold range (6 step
589 twofold dilutions) in 96 well plates. 100 µl asexual parasite culture (prepared in hypoxanthine-free
590 medium) were added to each well and mixed with the compound to obtain a final haematocrit of 1.25%
591 and a final parasitaemia of 0.3%. After incubation for 48 hrs, 0.25 µCi of [3H]-hypoxanthine was added
592 per well and plates were incubated for an additional 24 hrs. Parasites were then harvested onto glass-
593 fiber filters using a Microbeta FilterMate cell harvester (Perkin Elmer, Waltham, US) and radioactivity
594 was counted using a MicroBeta2 liquid scintillation counter (Perkin Elmer, Waltham, US). The results
595 were recorded and expressed as a percentage of the untreated controls. Curve fitting and IC50
596 calculations were performed using a non-linear, four-parameter regression model with variable
597 slope (Graph Pad Prism, version 8.2.1).

598

599 **4.7 Fluorescence microscopy**

600 To localize *Pf*FKBP35, NF54/iKD-FKBP35 parasites were fixed in 4% formaldehyde/0.0075%
601 glutaraldehyde for 30 min at room temperature and washed three times in PBS. The fixed cells
602 were permeabilized by incubation with 0.1% Triton-X100-containing PBS for 15 min. After
603 two washing steps in PBS, the cells were incubated in a blocking/aldehyde quenching solution
604 (3% BSA in PBS complemented with 50 mM ammonium chloride). The samples were
605 incubated with the primary antibodies rabbit α-GFP (1:400, Abcam ab6556) and mAb mouse
606 α-fibrillarin (1:100, Santa Cruz Biotechnology sc-166021) for 1 h in 3% BSA in PBS and
607 washed 3 times in PBS. Subsequently, the samples were incubated with the secondary
608 antibodies goat α-rabbit IgG (H&L) Alexa Fluor 488 (1:250, Invitrogen A11008) and goat α-
609 mouse IgG (H&L) Alexa Fluor 594 (1:250, Invitrogen A11032), for 1 h and washed 3 times,
610 before they were mixed with Vectashield containing DAPI (Vector laboratories, H-1200), and

611 mounted on a microscopy slide. Slides were imaged using a Leica THUNDER 3D Assay
612 imaging system.

613

614 **4.8 Proteomics**

615 Parasite cultures were split at 0-6 hpi in G1 and treated for 4 h with 100 nM rapamycin. Saponin
616 lysis of paired FKBP35^{WT} and FKBP35^{KO} populations at 36-42 hpi in G1 and 24-30 hpi in G2
617 was performed as described above. Samples were collected in three independent biological
618 replicates. The washed parasite pellet was snap frozen in liquid nitrogen. After thawing,
619 parasites were resuspended in 25 µL of lysis buffer (5% SDS, 100 mM tetraethylammonium
620 bromide (TEAB), 10 mM tris(2-carboxyethyl)phosphin (TCEP), pH 8.5) and sonicated (10
621 cycles, 30 sec on/off at 4 °C, Bioruptor, Diagnode). Lysates were subsequently reduced for 10
622 minutes at 95 °C. Samples were then cooled down to RT and 0.5 µL of 1M iodoacetamide was
623 added to the samples. Cysteine residues were alkylated for 30 min at 25 °C in the dark.
624 Digestion and peptide purification was performed using S-trap technology (Protifi) according
625 to the manufacturer's instructions. In brief, samples were acidified by addition of 2.5 µL of
626 12% phosphoric acid (1:10) and then 165 µL of S-trap buffer (90% methanol, 100 mM TEAB
627 pH 7.1) was added to the samples (6:1). Samples were briefly vortexed and loaded onto S-trap
628 micro spin-columns (Protifi) and centrifuged for 1 min at 4000 g. Flow-through was discarded
629 and spin-columns were then washed 3 times with 150 µL of S-trap buffer (each time samples
630 were centrifuged for 1 min at 4000 g and flow-through was removed). S-trap columns were
631 then moved to the clean tubes and 20 µL of digestion buffer (50 mM TEAB pH 8.0) and trypsin
632 (at 1:25 enzyme to protein ratio) were added to the samples. Digestion was allowed to proceed
633 for 1h at 47 °C. Then, 40 µL of digestion buffer were added to the samples and the peptides
634 were collected by centrifugation at 4000 g for 1 minute. To increase the recovery, S-trap
635 columns were washed with 40 µL of 0.2% formic acid in water (400g, 1 min) and 35 µL of
636 0.2% formic acid in 50% acetonitrile. Eluted peptides were dried under vacuum and stored at -
637 20 °C until further analysis.

638 Peptides were resuspended in 0.1% aqueous formic acid and peptide concentration was adjusted
639 to 0.25 µg/µL. 1 µL of each sample was subjected to LC-MS/MS analysis using an Orbitrap
640 Elicpse Tribrid Mass Spectrometer fitted with an Ultimate 3000 nano system (both from
641 Thermo Fisher Scientific) and a custom-made column heater set to 60 °C. Peptides were
642 resolved using a RP-HPLC column (75 µm × 30 cm) packed in-house with C18 resin (ReproSil-

643 Pur C18–AQ, 1.9 µm resin; Dr. Maisch GmbH) at a flow rate of 0.3 µL/min. The following
644 gradient was used for peptide separation: from 2% buffer B to 12% B over 5 min, to 30% B
645 over 40 min, to 50% B over 15 min, to 95% B over 2 min followed by 11 min at 95% B then
646 back to 2% B. Buffer A was 0.1% formic acid in water and buffer B was 80% acetonitrile, 0.1%
647 formic acid in water.

648 The mass spectrometer was operated in DDA mode with a cycle time of 3 seconds between
649 master scans. Each master scan was acquired in the Orbitrap at a resolution of 240,000 FWHM
650 (at 200 m/z) and a scan range from 375 to 1600 m/z followed by MS2 scans of the most intense
651 precursors in the linear ion trap at "Rapid" scan rate with isolation width of the quadrupole set
652 to 1.4 m/z. Maximum ion injection time was set to 50 ms (MS1) and 35 ms (MS2) with an AGC
653 target set to 1e6 and 1e4, respectively. Only peptides with charge state 2-5 were included in the
654 analysis. Monoisotopic precursor selection (MIPS) was set to Peptide, and the Intensity
655 Threshold was set to 5e3. Peptides were fragmented by HCD (Higher-energy collisional
656 dissociation) with collision energy set to 35%, and one microscan was acquired for each
657 spectrum. The dynamic exclusion duration was set to 30 seconds.

658 The acquired raw-files were imported into the Progenesis QI software (v2.0, Nonlinear
659 Dynamics Limited), which was used to extract peptide precursor ion intensities across all
660 samples applying the default parameters. The generated mgf-file was searched using MASCOT
661 against a *Plasmodium falciparum* (isolate 3D7) database (Uniprot, 11.2019) and 392 commonly
662 observed contaminants using the following search criteria: full tryptic specificity was required
663 (cleavage after lysine or arginine residues, unless followed by proline); 3 missed cleavages were
664 allowed; carbamidomethylation (C) was set as fixed modification; oxidation (M) and acetyl
665 (Protein N-term) were applied as variable modifications; mass tolerance of 10 ppm (precursor)
666 and 0.6 Da (fragments). The database search results were filtered using the ion score to set the
667 false discovery rate (FDR) to 1% on the peptide and protein level, respectively, based on the
668 number of reverse protein sequence hits in the dataset. Quantitative analysis results from label-
669 free quantification were processed using the SafeQuant R package v.2.3.2 (69) to obtain peptide
670 relative abundances. This analysis included global data normalization by equalizing the total
671 peak/reporter areas across all LC-MS runs, data imputation using the knn algorithm, summation
672 of peak areas per protein and LC-MS/MS run, followed by calculation of peptide abundance
673 ratios. Only isoform specific peptide ion signals were considered for quantification. To meet
674 additional assumptions (normality and homoscedasticity) underlying the use of linear
675 regression models and t-Tests, MS-intensity signals were transformed from the linear to the

676 log-scale. The summarized peptide expression values were used for statistical testing of
677 between condition differentially abundant peptides. Here, empirical Bayes moderated t-Tests
678 were applied, as implemented in the R/Bioconductor limma package (70). The resulting per
679 protein and condition comparison *p*-values were adjusted for multiple testing using the
680 Benjamini-Hochberg method.

681 Gene ontology enrichment analysis was performed using the PANTHER Overrepresentation
682 Test with the correction method "False Discovery Rate", the test type "Fisher's Exact", and the
683 annotation data set "PANTHER GO-Slim" (37).

684

685 **4.9 IPP complementation**

686 Parasite cultures were split at 0-6 hpi in G1 and treated for 4 h with 100 nM rapamycin.
687 FKBP35^{KO} and FKBP35^{WT} populations were split again and supplemented either with 200 µM
688 isopentenyl pyrophosphate (IPP) (Sigma I0503) or the corresponding volume H_2O. The
689 respective culture medium was replaced daily. Parasites treated with 156 ng/mL doxycycline
690 (Sigma D9891) were used to confirm that IPP complementation is able to rescue apicoplast-
691 deficient parasites. DNA content analysis was performed as described above.

692

693 **4.10 Heat shock susceptibility testing**

694 Parasites cultures were split at 0-6 hpi in G1 and treated for 4 h with 100 nM rapamycin. While
695 control populations were always incubated at 37 °C, test populations were incubated at 40 °C
696 for 6 h starting at 24-30 hpi. Parasitaemia was measured in G2 using flow cytometry as
697 described above.

698

699 **4.11 Surface sensing of translation (SUnSET)**

700 Parasite cultures were split at 0-6 hpi in G1 and treated for 4 h with 100 nM rapamycin. At 24-
701 30 hpi in G2, the cultures were incubated with 1 µg/mL puromycin (Sigma P8833) for 1 h at
702 37 °C (41, 71). Saponin lysis and Western blotting were performed as described above.

703

704 **4.12 Cellular thermal shift assay (CETSA)**

705 The mass spectrometry-based isothermal dose-response cellular thermal shift assay (ITDR-MS-
706 CETSA) was performed according to the protocol developed by Dziekan and colleagues (47).
707 Briefly, live parasites (10^7 MACS-purified trophozoites per condition) were exposed to a
708 FK506 (MedChemExpress HY-13756) concentration gradient (100 µM to 1.5 nM) and a
709 DMSO control for 1 h. Subsequently, the parasites were washed in PBS and exposed to the
710 denaturing temperatures 50 °C, 55 °C and 60 °C as well as to a non-denaturing temperature 37
711 °C for 3 min, before they were cooled down to 4 °C for 3 min. Afterwards, the cells were lysed
712 by resuspending in a lysis buffer (50 mM HEPES pH 7.5, 5 mM β-glycerophosphate, 0.1 mM
713 Na_3VO_4, 10 mM $MgCl_2$, 2 mM TCEP, and EDTA-free protease inhibitor cocktail (Sigma)),
714 three freeze/thaw cycles, and mechanical shearing using a syringe with a 31-gauge needle.
715 Subsequently, insoluble proteins were pelleted by centrifugation (20 min at 4 °C and 20'000 g)
716 and the soluble fraction was collected and subjected to protein digestion, reduction, alkylation,
717 and TMT10 labelling followed by LC/MS analysis as described (47).

718 To prepare the protein lysate, saponin-lysed parasites were lysed in the afore-mentioned buffer
719 by three freeze/thaw cycles and mechanical shearing. After centrifugation, soluble proteins
720 were exposed to a FK506 concentration gradient (200 µM to 3 nM) and a DMSO control for 1
721 min before the thermal challenge was performed as described above. Afterwards, the soluble
722 protein fraction was isolated and prepared for by LC/MS analysis as described (47).

723 Data analysis was performed using the Proteome Discoverer 2.1 software (Thermo Fisher
724 Scientific) and the R package "mineCETSA" (v 1.1.1). Only proteins identified by at least three
725 peptide spectrum matches (PSMs) were included in the analysis (47).

726

727 **4.13 Transcriptomics**

728 **4.13.1 Sample preparation**

729 The RNA of 500 µL iRBCs at 3-5% parasitaemia was isolated using 3 mL TRIzol reagent
730 (Invitrogen) followed by phenol-chloroform phase separation. The aqueous phase was purified
731 using the Direct-zol RNA MicroPrep kit (Zymo). Samples were collected from three biological
732 replicates. Stranded RNA sequencing libraries were prepared using the Illumina TruSeq
733 stranded mRNA library preparation kit (REF 20020594) according to the manufacturer's
734 protocol. The library was sequenced in 100 bp paired-end reads on an Illumina NextSeq 2000

735 sequencer using the Illumina NextSeq 2000 P3 reagents (REF 20040560), resulting in 5 million
736 reads on average per sample.

737 **4.13.2 RNA-Seq data analysis**

738 Fastqc was run on all raw fastq files. Then, each file was aligned with hisat2 (version 2.0.5)
739 (72) against the 3D7 reference genome (PlasmoDB v58) (73) in which the GFP and the recoded
740 FBPK35 sequences were added at the end of chromosome 12. Read counts for each gene and
741 for each sample were then counted using featureCount (gff file from PlasmoDB v58 modified
742 to include the added GFP and FBPK35). TPM (Transcripts Per Kilobase Million) were then
743 calculated from the raw count matrix.

744 Principal component analysis (PCA) was performed using the R (version 4.2.1) function
745 prcomp using log transformed TPMs. PCA revealed that the rapamycin-treated replicate B of
746 TP 3 ("3B.R") was a clear outlier and is different from any other replicate at any time point
747 (Fig. S3D). For this reason, it was excluded from further analysis. The PCA was done again
748 without it and the other samples show the same pattern as the initial PCA (Fig. S3E).

749 DESeq2 (version 1.36) (74) was used for normalization and differential expression analysis.
750 Paired differential expression tests where done for each time point using DESeq2 LRT
751 (likelihood ratio test) using the full model ~ Treatment + Replicate (Treatment is DMSO or
752 Rapamycin and Replicate is the clone, added as the data is paired) and the reduced model ~
753 Replicate. From this paired test and the average log fold-change calculated from the TPMs,
754 normalized volcano plots were made using the R package EnhancedVolcano (version 1.14)
755 (75).

756 **4.13.3 Cell cycle analysis**

757 Spearman correlation between normalized scaled read counts for each sample for all genes (as
758 one vector) and each time point of the reference microarray time course published by Bozdech
759 *et al*. (42) (3D7 smoothed, retrieved from PlasmoDB) were tested. Spearman's coefficients rho
760 for each time point of this RNA-Seq time course and each time point of the reference data set
761 where plotted using ggcorrplot (version 0.1.3) (76). For each time point of this RNA-Seq
762 dataset, the rho coefficients where then plotted against the time points of the reference data set
763 and the FKBP35^{WT} and FKBP35^{KO} data were fitted separately to the linearized sinusoidal $A *$
764 $sin\left(\frac{2\pi}{53}time\right) + B * cos\left(\frac{2\pi}{53}time\right) + C$ using R lm function. The time point matching best to
765 the FKBP35$^{\mathbf{WT}}$ and FKBP35$^{\mathbf{KO}}$ samples for each time point of the RNA-Seq time course was

766 taken as the maximum of this fitted function. Both fitted functions were F-tested (using R
767 function var.test using both fitted model as applied to the FKBP35^{KO} data) to test whether the
768 FKBP35^{WT} and FKBP35^{KO} data correlated with the reference data set (42) in a significantly
769 different way, which would indicate a cell cycle shift if statistically significant. Only the last
770 time point showed such a significant difference.

771

772 **Data availability**

773 The mass spectrometry proteomics data have been deposited to the ProteomeXchange
774 Consortium repository with the dataset identifier PXD039018. The sequencing data are
775 available in the Sequence Read Archive (SRA) via the accession number PRJNA914079.

776

777 **Acknowledgements**

778 We thank Vera Mitesser and Ron Dzikowski for guidance on the SUnSET experiments and
779 David Fidock for providing the parasite line Dd2-B2 used for the attempted resistance selection.
780 We are grateful to the Polyomics facility at the University of Glasgow for processing the
781 samples for RNA-Seq. This work was supported by the Swiss National Foundation (grant
782 number 310030_200683), the Wolfson Merit Royal Society Award, the Wellcome Trust
783 Investigator Award 110166 and Wellcome Trust Center Award 104111, and by the Singapore
784 Ministry of Education (grant number MOE-T2EP30120-0015).

785

786 **Author contributions**

787 B.T.T. designed and performed experiments, analyzed and interpreted the data, and wrote the
788 original draft of the manuscript. J.M.D. and S.T. performed and interpreted CETSA
789 experiments. Z.B. supervised these experiments and provided resources. F.A. analyzed RNA-
790 Seq data. M.M. supervised these experiments and provided resources for RNA-Seq data
791 generation. A.P. performed immunofluorescence assays. K.B. performed and analyzed
792 proteomics experiments supervised by A.S. C.Gu. and M.R. performed and interpreted
793 hypoxanthine incorporation assays. C.Gr. edited the manuscript. N.M.B.B. conceived the study,
794 designed and supervised experiments, provided resources, and wrote the manuscript. All
795 authors contributed to the final editing of the manuscript.

796

797 **Declaration of interests**

798 The authors declare that they have no conflict of interest.

799

800 **Figures**

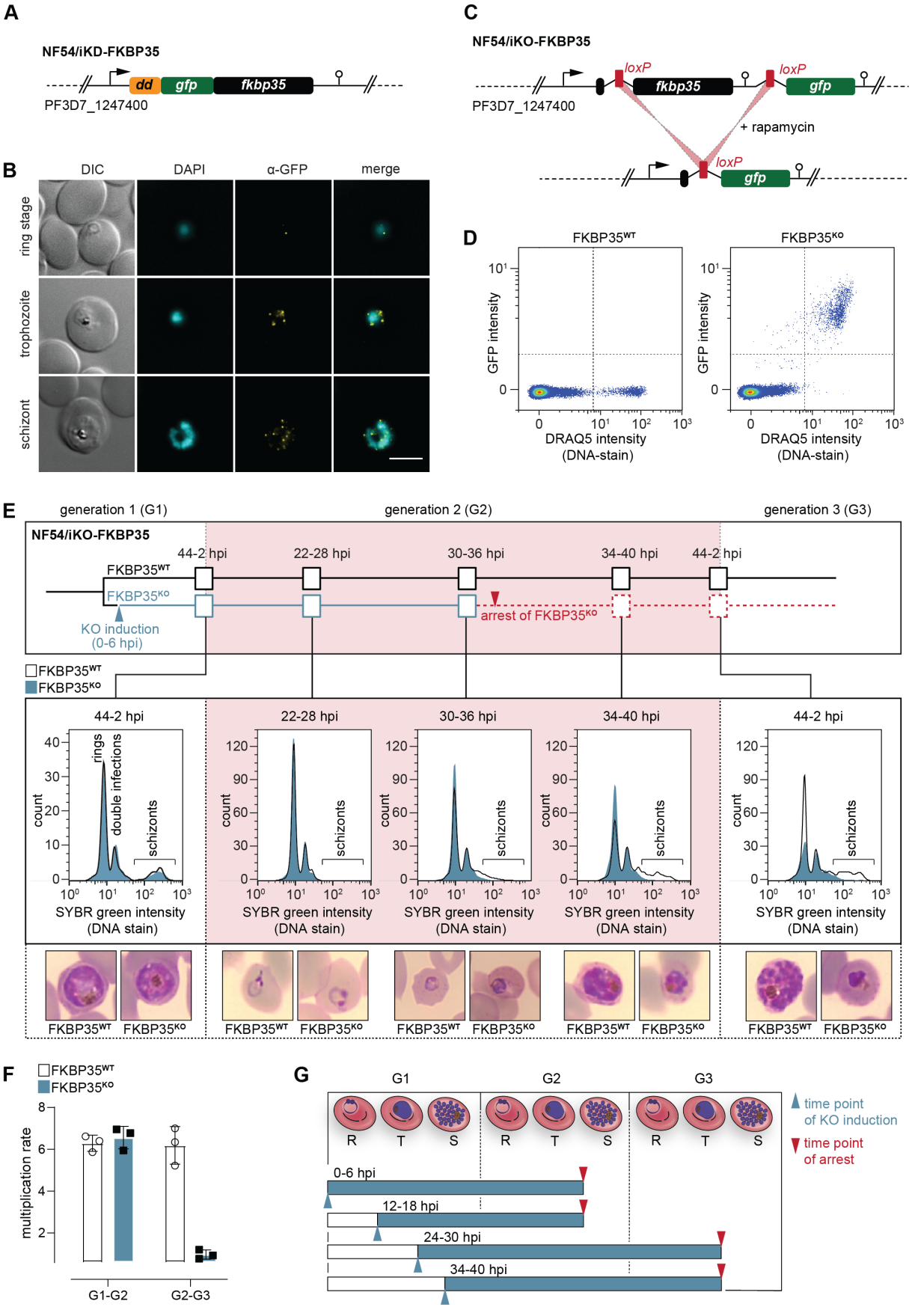

801

802

803 **Figure 1. *Pf*FKBP35 depletion causes delayed parasite death.**

804 **(A)** Schematic of the N-terminally modified *fkbp35* locus in NF54/iKD-FKBP35 parasites. *dd*,
805 destabilization domain. *gfp*, *green fluorescent protein*. **(B)** Localization of *Pf*FKBP35 in
806 NF54/iKD-FKBP35 parasites at the ring, trophozoite and schizont stage assessed by
807 immunofluorescence. DNA was stained with DAPI. Representative images are shown. Scale
808 bar: 5 µm. DIC, differential interference contrast. **(C)** Schematic of the modified *fkbp35* locus
809 in NF54/iKO-FKBP35 parasites before and after *loxP* recombination. *gfp*, *green fluorescent*
810 *protein*. **(D)** Flow cytometry plot showing GFP expression in G1 schizonts of FKBP35$^{\mathbf{KO}}$ and
811 FKBP35$^{\mathbf{WT}}$. DNA was stained with DRAQ5. **(E)** Time course showing the development of
812 NF54/iKO-FKBP35 parasites. Upper panel: Schematic of the experimental setup. Middle
813 panel: DNA content of the populations assessed by flow cytometry based on the SYBR Green
814 intensity. Lower panel: Giemsa-stained blood smears. The knockout was induced at 0-6 hpi.
815 Representative data of three biological replicates are shown. **(F)** Multiplication rates of
816 FKBP35$^{\mathbf{KO}}$ and FKBP35$^{\mathbf{WT}}$ parasites from generation 1 to generation 2 (G1-G2) and G2-G3.
817 The knockout was induced at 0-6 hpi. Multiplication rates were determined using flow
818 cytometry. Data points represent the multiplication rates from G1-G2 and G2-G3. n=3, error
819 bars represent the standard error of the mean. **(G)** Schematic showing time point of growth
820 arrest (red arrow) following *Pf*FKBP35 knock-out at different hpi (blue arrow). R, ring stage;
821 T, trophozoite stage; S, schizont stage.
822

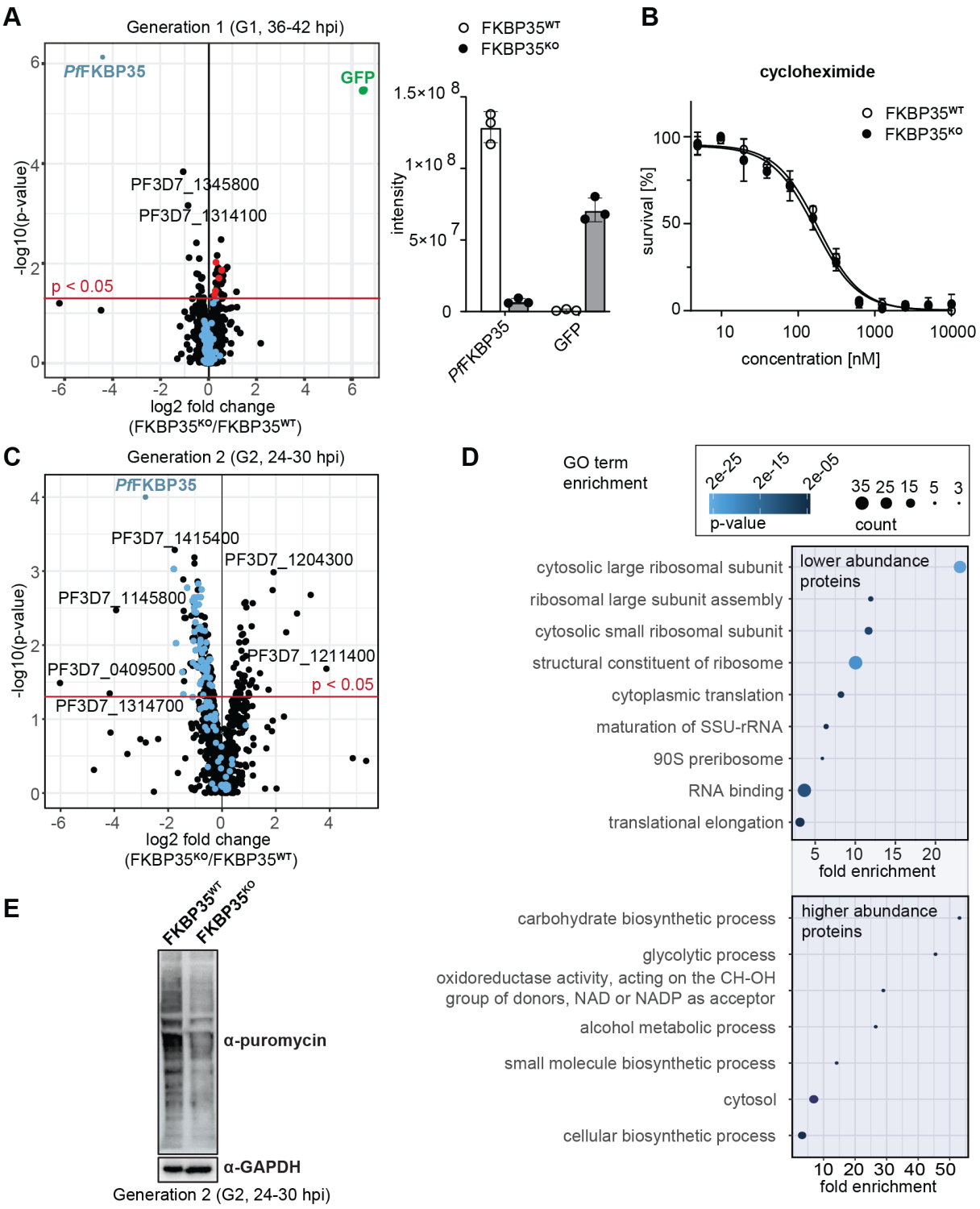

Figure 2. *Pf*FKBP35 is crucial for ribosome homeostasis and protein synthesis.

(A) Left panel: Proteome analysis of schizonts (36-42 hpi) in G1. The volcano plot shows change in protein abundance in FKBP35^{KO} compared to FKBP35^{WT}. Ribosomal proteins are highlighted in blue, proteins associated with the GO terms "pre-ribosome" or "nucleolus" in red. n=3. Right panel: Relative difference in *Pf*FKBP35 and GFP abundance expressed as signal intensity measured by mass spectrometry. n=3, error bars represent the standard error of the

830 mean. **(B)** Dose-response effect of the translation inhibitor cycloheximide on FKBP35^{KO} and
831 FKBP35^{WT} parasites. The knockout was induced at 0-6 hpi and parasites were subsequently
832 exposed to cycloheximide for 48 h. Parasite survival was quantified by flow cytometry. n=3,
833 error bars represent the standard error of the mean. **(C)** Proteome analysis of trophozoites (24-
834 30 hpi) in G2. The volcano plot shows change in protein abundance in FKBP35^{KO} compared to
835 FKBP35^{WT}. Ribosomal proteins are highlighted in blue. n=3. **(D)** GO enrichment analysis of
836 significantly deregulated proteins in FKBP35^{KO} trophozoites in G2. GO enrichment analysis
837 was performed using the PANTHER "Overrepresentation Test" with the test type "Fisher's
838 Exact" and the correction method "False Discovery Rate". **(E)** Assessment of translation
839 activity using SUnSET. FKBP35^{KO} and FKBP35^{WT} trophozoites of G2 were incubated with
840 puromycin for 1 hour. Incorporated puromycin was detected using an α-puromycin antibody.
841 α-GAPDH served as loading control. n=3, a representative Western blot is shown.
842

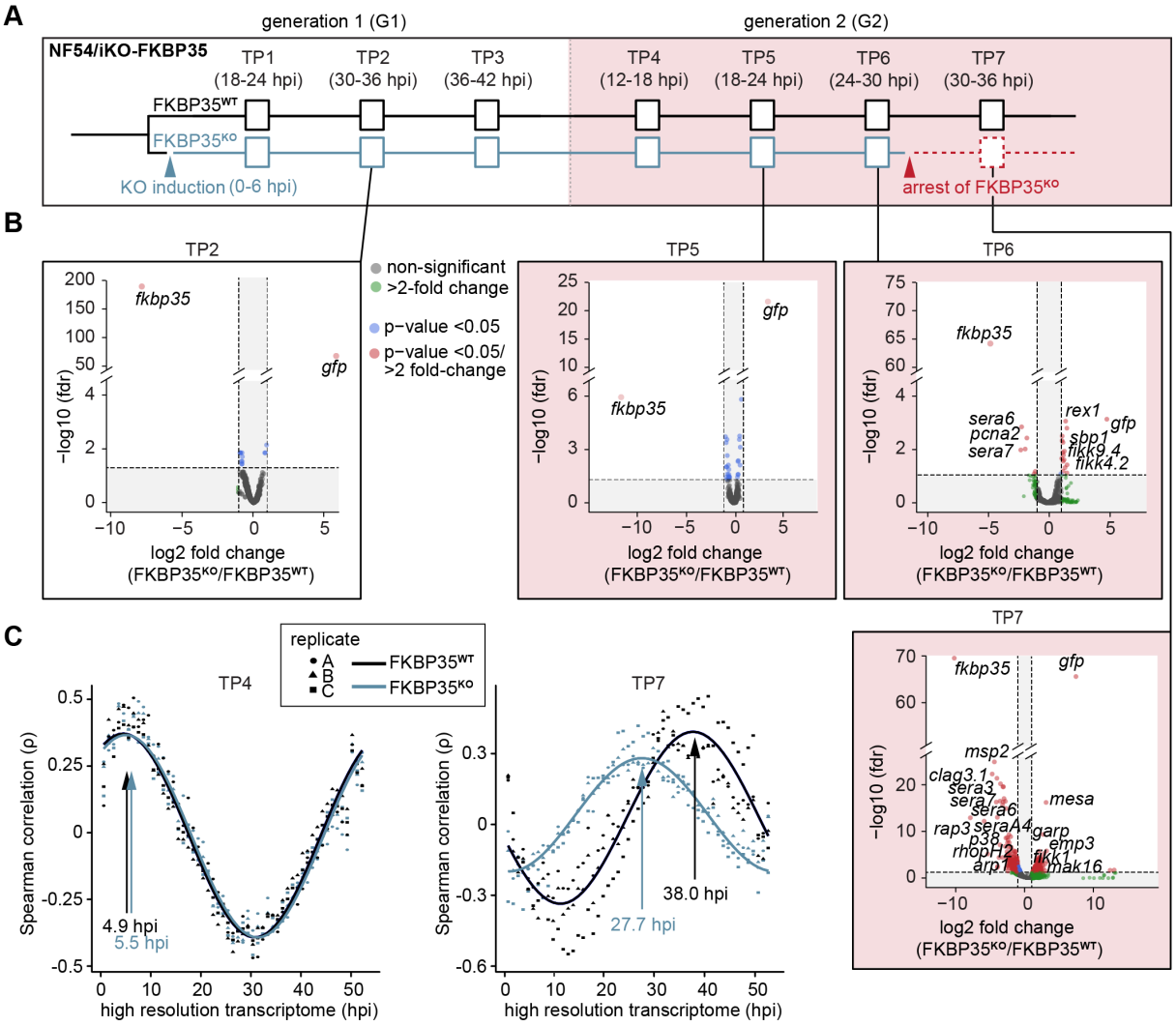

Figure 3. The knockout of *Pf*FKBP35 remains silent at the transcriptomic level.

(A) Setup of the RNA-Seq experiment. RNA was collected at seven indicated time points (TP). **(B)** Volcano plots show differential gene expression between FKBP35^{KO} and FKBP35^{WT} parasites. Genes are color-coded according to the fold change and fdr (false discovery rate), n=3. **(C)** Mapping of FKBP35^{KO} and FKBP35^{WT} transcriptomes to a high-resolution reference (42). Spearman rank coefficients (ρ) show correlation between the sampled transcriptomes and the reference data set (42). The time points with the highest correlation coefficient are indicated.

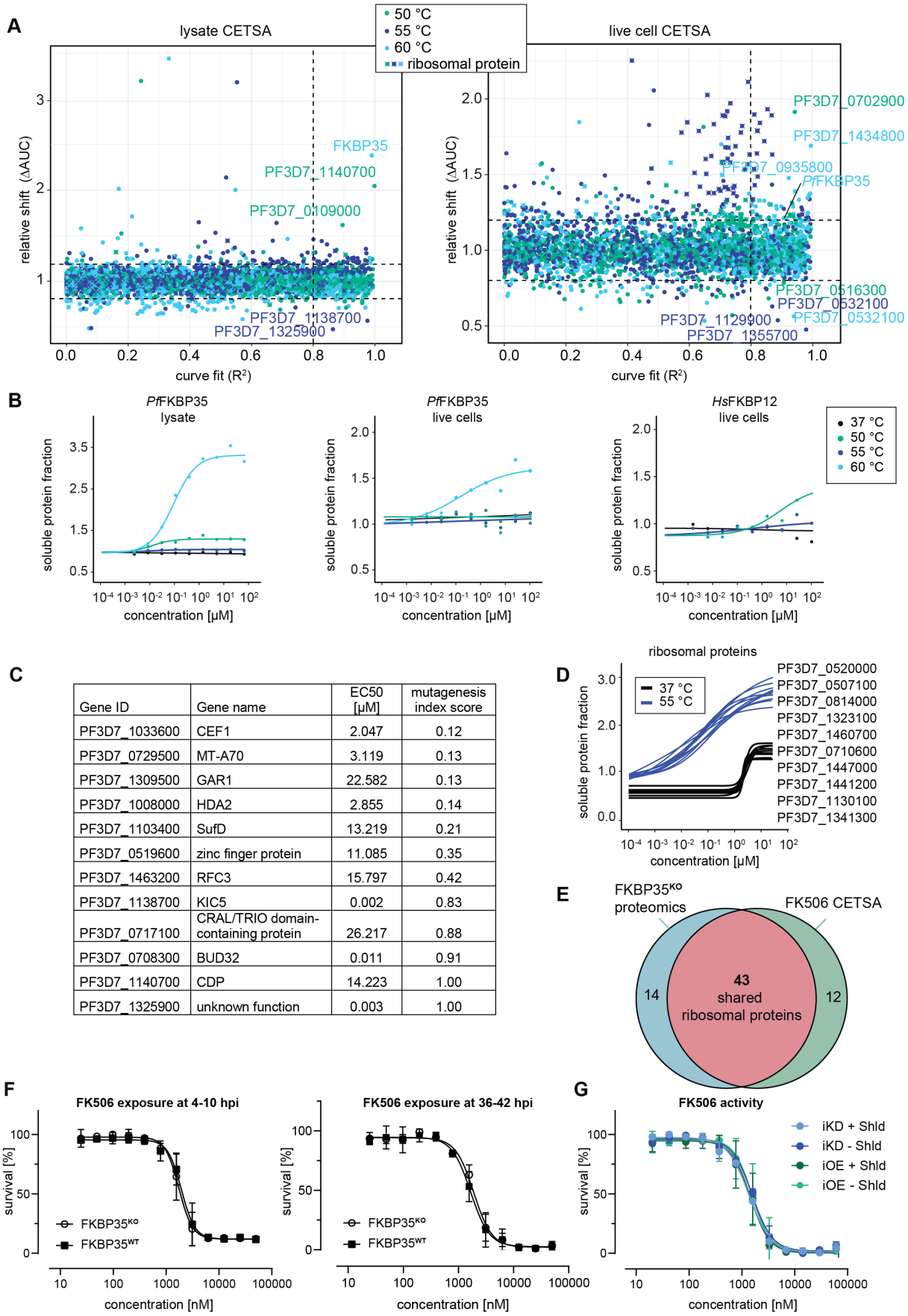

Gene ID	Gene name	EC50 [µM]	mutagenesis index score
PF3D7_1033600	CEF1	2.047	0.12
PF3D7_0729500	MT-A70	3.119	0.13
PF3D7_1309500	GAR1	22.582	0.13
PF3D7_1008000	HDA2	2.855	0.14
PF3D7_1103400	SufD	13.219	0.21
PF3D7_0519600	zinc finger protein	11.085	0.35
PF3D7_1463200	RFC3	15.797	0.42
PF3D7_1138700	KIC5	0.002	0.83
PF3D7_0717100	CRAL/TRIO domain-containing protein	26.217	0.88
PF3D7_0708300	BUD32	0.011	0.91
PF3D7_1140700	CDP	14.223	1.00
PF3D7_1325900	unknown function	0.003	1.00

Figure 4. CETSA identifies FK506 interaction partners.

854 **(A)** CETSA results. The relative shift in protein abundance (area under the curve of heat-
855 challenged samples normalized against the non-denaturing control, ΔAUC) as a function of R^2
856 (goodness of fit as a measure for the dose-response effect). The dashed lines indicate an
857 arbitrary cutoff of 3 times the median absolute deviation (MAD) of each dataset and R^2=0.8.
858 Three different temperatures were used for protein denaturation (indicated by colors). **(B)** Dose-
859 dependent stabilization of *P. falciparum* and human FKBPs detected using lysate and live cell
860 CETSA. Bullets represent the abundance of non-denatured proteins in response to increasing
861 FK506 concentrations under thermal challenge relative to the DMSO control. Colors indicate
862 the temperatures used for heat challenge; the black curve represents the non-denaturing (37°C)
863 control. **(C)** Proteins with the most pronounced stability shift under thermal challenge in the
864 lysate CETSA experiment are listed. The EC50 is the concentration at which the half-maximal
865 effect of the FK506-induced thermal stabilization is reached. The mutagenesis index score
866 determined by Zhang *et al*. (18) is a measure to predict if a protein is essential for asexual
867 growth: 0=essential, 1=non-essential. **(D)** Fitted live cell CETSA curves of 10 representative
868 ribosomal proteins at 37 °C and 55 °C. Ribosomal proteins show a FK506 dose-dependent
869 increase in soluble protein fraction. **(E)** Venn diagram showing the overlap between ribosomal
870 proteins deregulated in the *Pf*FKBP35 knock-out cell line (less abundant in G2 FKBP$^{\mathbf{KO}}$
871 trophozoites determined by proteomics) and the ribosomal proteins stabilized by FK506 in live
872 cell CETSA. The number of factors identified in either or both assays is indicated. **(F)** Dose-
873 response effect of FK506 on FKBP35$^{\mathbf{KO}}$ and FKBP35$^{\mathbf{WT}}$ parasites. The knockout was induced
874 at 0-6 hpi and parasites were exposed to FK506 at 4-10 hpi (left panel) and 36-42 hpi in G1
875 (right panel). Parasite survival was measured after reinvasion (10-16 hpi) in G2. n=3, error bars
876 represent the standard error of the mean. **(G)** Dose-response effect of FK506 on NF54/iKD-
877 FKBP35 and NF54/iOE-FKBP35 parasites in presence and absence of Shield-1 (Shld).
878 Parasites were split at 0-6 hpi and subsequently treated with Shld or the vehicle control EtOH.
879 Data points represent the mean of three and two independent biological replicates for the
880 NF54/iOE-FKBP35 and NF54/iKD-FKBP35 cell line, respectively. Error bars represent the
881 standard error of the mean.
882

883 **Supplemental figures**

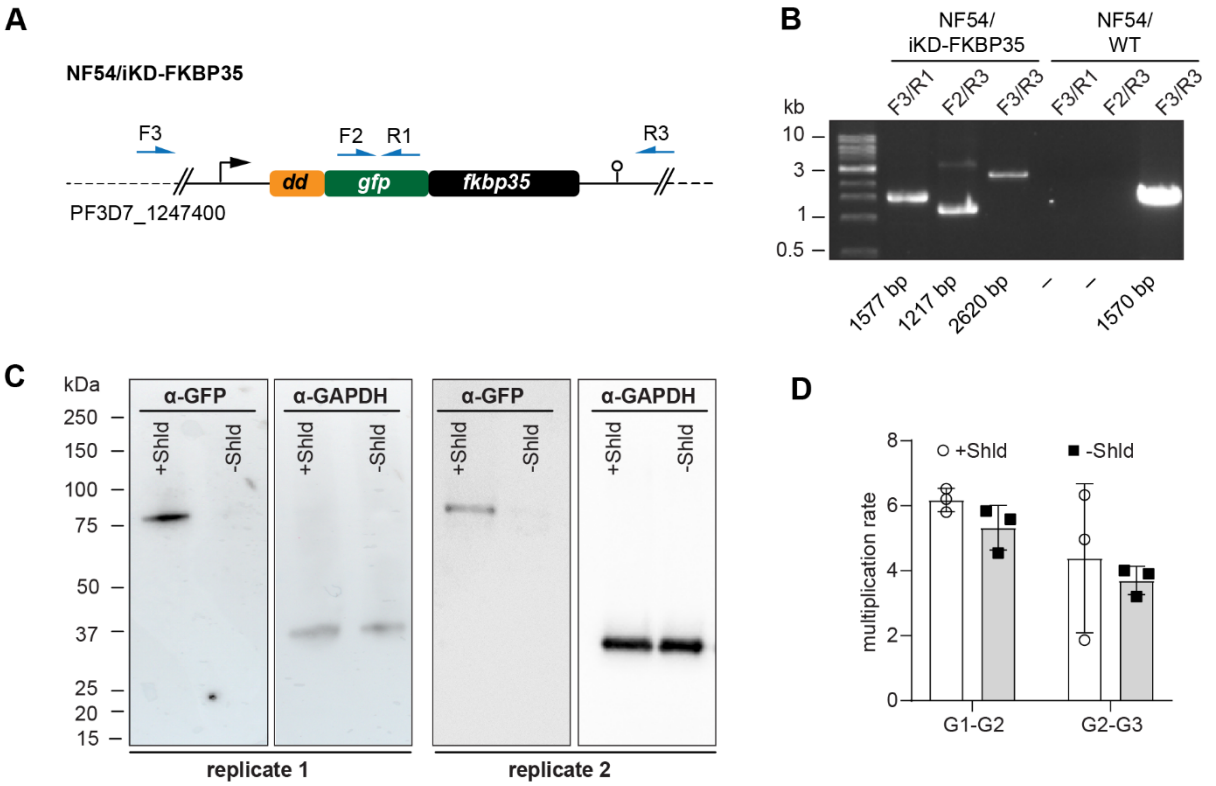

884

885 **Figure S1. Characterization of NF54/iKD-FKBP35 parasites.**

886 **(A)** Schematic of the modified *fkbp35* locus (PF3D7_1247400) in NF54/iKD-FKBP35
887 parasites. The 5'-end of *fkbp35* was tagged with the sequences of a destabilization domain (*dd*)
888 and a green fluorescent protein (*gfp*). The DD tag allows regulating protein levels post-
889 translationally using the stabilizing compound Shield-1 (Shld) (30, 31). Names and binding
890 sites of the primers used for diagnostic PCRs are indicated. **(B)** Diagnostic PCRs performed on
891 gDNA of NF54/FKBP35 iKD parasites to confirm correct editing of the locus. PCRs performed
892 on NF54/WT gDNA served as control. Numbers at the bottom indicate expected fragement
893 sizes. **(C)** Expression levels of the DD-GFP-FKBP35 fusion protein were assessed by Western
894 blot. Parasite cultures were split at 0-6 hpi and treated with Shld or the vehicle control EtOH.
895 Protein lysates were collected 40 hours later. α-GAPDH served as loading control. The expected
896 size of the DD-GFP-FKBP35 fusion protein is 74.2 kDa. **(D)** Multiplication rates of NF54/iKD-
897 FKBP35 parasites from generation 1 to generation 2 (G1-G2) and G2-G3. Parasites were split
898 at 0-6 hpi and treated with Shld or the vehicle control EtOH. Multiplication rates were
899 determined using flow cytometry. Data points represent the multiplication rates from G1-G2
900 and G2-G3, respectively. n=3; error bars represent the standard error of the mean.

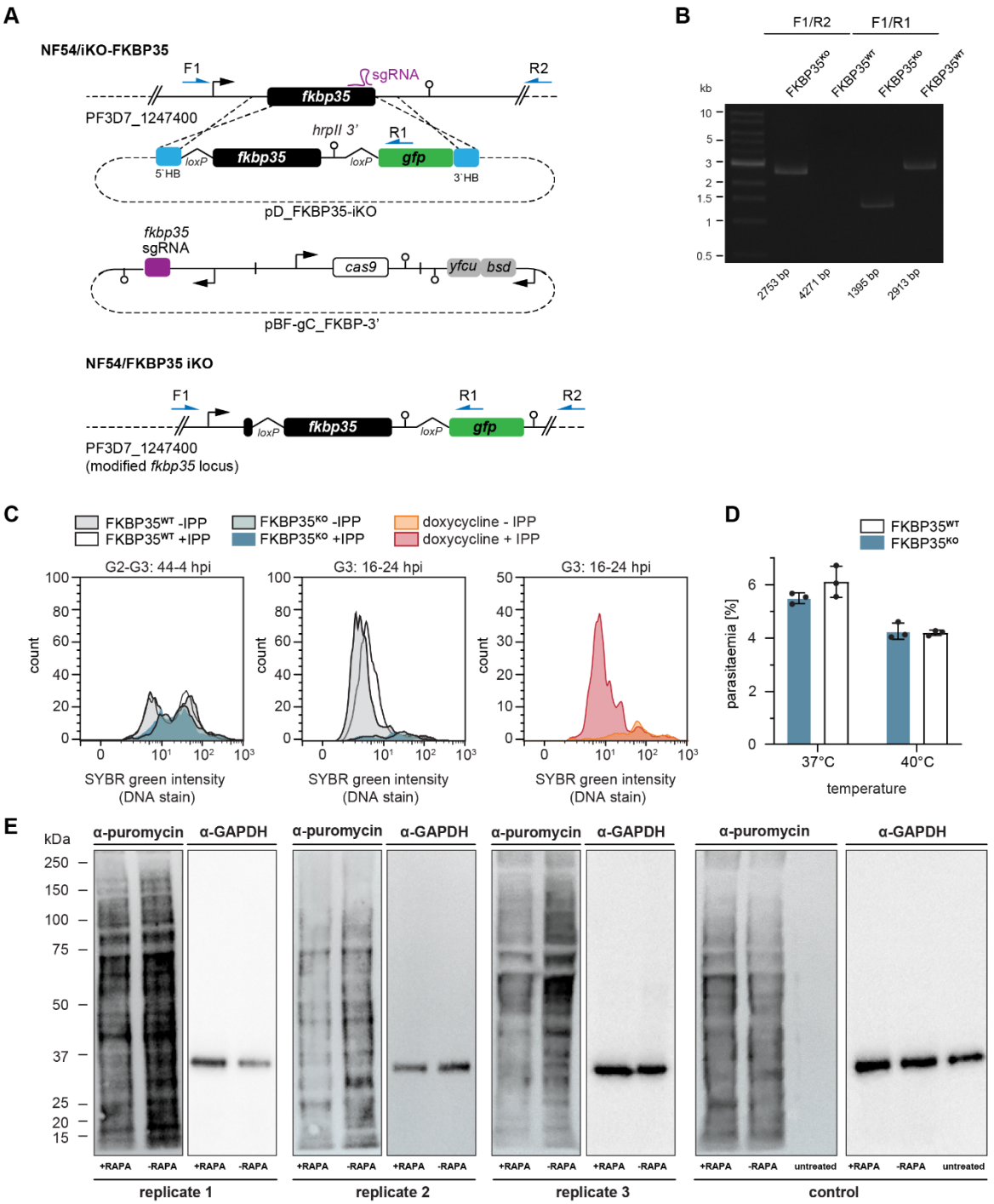

Figure S2. CRISPR/Cas9-based generation of transgenic parasite lines.

(A) Schematic of the wild type *fkbp35* locus (PF3D7_1247400) and the two plasmids used for CRISPR/Cas9 gene editing (pD_FKBP35-iKO and pBF-gC_FKBP-3') to generate the modified *fkbp35* locus of NF54/iKO-FKBP35 parasites. The modification consists of an intron containing a *loxP* site that was introduced after the first 38 bp of the coding sequence and an *hrpII* terminator inserted after the stop codon followed by another *loxP* site and a *gfp* sequence. The sequence flanked by the *loxP* sites was recodonized to prevent homologous recombination during gene editing. Names and binding sites of the primers used for diagnostic PCRs are

910 indicated. **(B)** Diagnostic PCRs on gDNA of NF54/iKO-FKBP35 parasites confirm correct
911 locus editing and rapamycin-induced *loxP* recombination. Numbers at the bottom indicate the
912 expected band sizes. **(C)** DNA content analysis of FKBP35$^{\mathbf{KO}}$ and FKBP35$^{\mathbf{WT}}$ parasites in
913 presence or absence of isopentenyl pyrophosphate (IPP)-supplementation. Disruption of
914 isoprenoid precursor biosynthesis in the apicoplast – the only essential function of this organelle
915 – is a known cause for delayed death in *P. falciparum* (35, 36). Inhibition of isoprenoid
916 synthesis by doxycycline can thus be restored by supplementing the parasite culture medium
917 with the isoprenoid precursor IPP (77). However, IPP supplementation did not alter the fate of
918 FKBP35$^{\mathbf{KO}}$ cells, demonstrating that their death in G2 is independent of apicoplast-dependent
919 processes as shown by DNA content analysis. Doxycycline-treated wild-type parasites rescued
920 by IPP-supplementation served as positive control**.** The knockout was induced at 0-6 hpi.
921 Representative data of three biological replicates are shown. **(D)** Parasite survival after
922 exposure to 40 °C for 6 h. Given the reported interactions of *Pf*FKBP35 with heat shock protein
923 70 (HSP70) and HSP90 (14, 16), we tested the parasite`s response to heat stress. *Pf*HSP70 is
924 required to ensure parasite survival under heat shock conditions by stabilizing the digestive
925 vacuole membrane trough binding to phosphatidylinositol 3-phosphate (78). Despite this
926 association, we did not detect altered heat-susceptibility between FKBP35$^{\mathbf{KO}}$ and FKBP35$^{\mathbf{WT}}$
927 cells. The knockout was induced at 0-6 hpi. n=3, error bars represent the standard error of the
928 mean**. (E)** Assessment of translation rates using SUnSET. FKBP35^{KO} and FKBP35^{WT}
929 trophozoites of G1 were incubated with puromycin for 1 hour. Incorporated puromycin was
930 detected using an α-puromycin antibody; α-GAPDH served as loading control. Replicate 3 is
931 also shown in main figure 3 (mirrored). The control was performed using an NF54/DiCre
932 parasite line. Untreated control parasites were cultured in absence of puromycin, confirming
933 the specificity of the α-puromycin antibody.

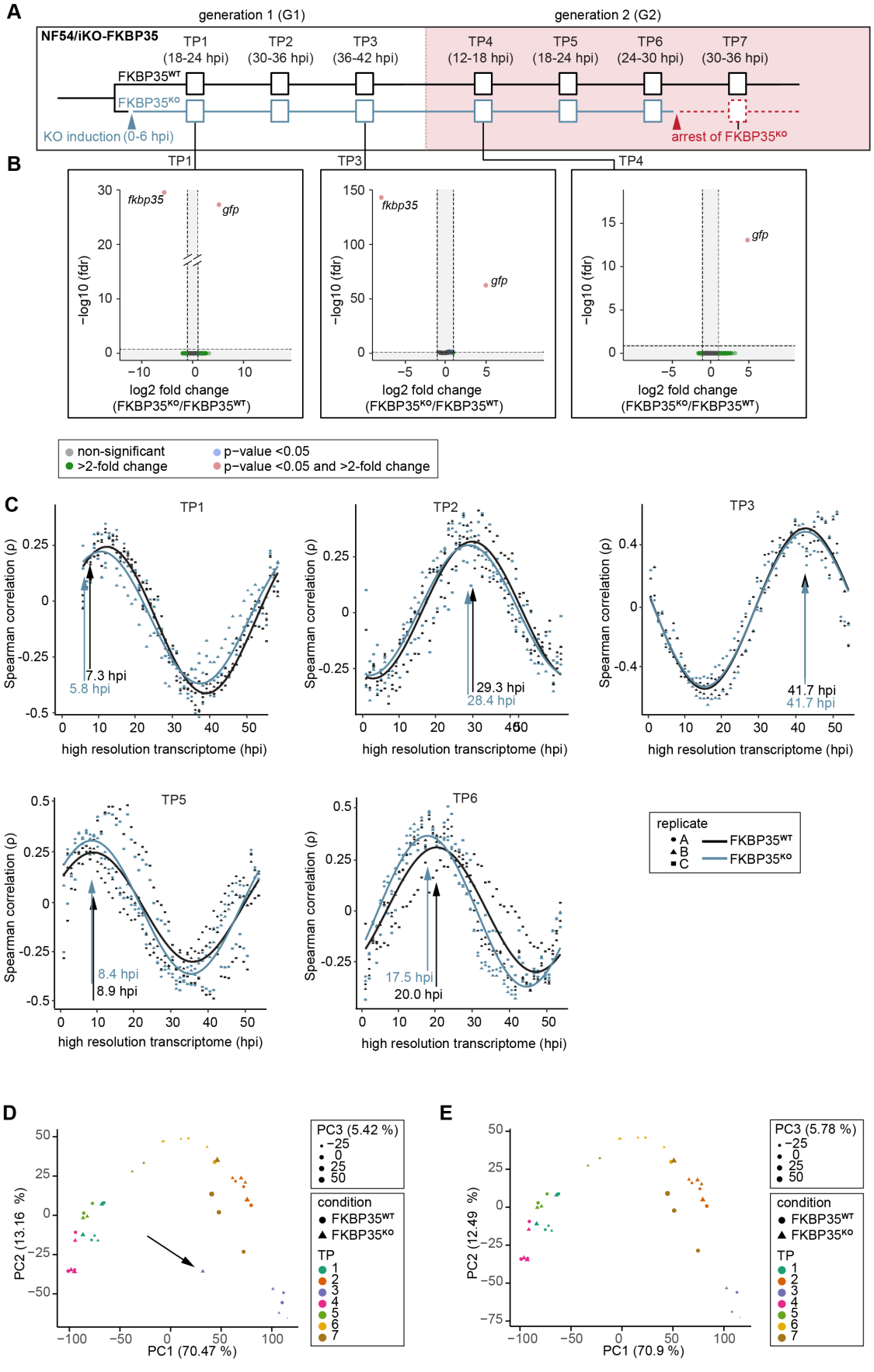

Figure S3. Transcriptomics reveals a cell cycle arrest of FKBP35^{KO} parasites.

936 **(A)** Schematic of the experimental setup. The knockout was induced at 0-6 hpi. RNA was
937 collected at indicated time points (TPs). **(B)** Volcano plots show differential gene expression
938 between $FKBP35^{KO}$ and $FKBP35^{WT}$ parasites. Genes are color-coded according to the fold
939 change and fdr (false discovery rate), n=3. **(C)** Mapping of $FKBP35^{\mathbf{KO}}$ and $FKBP35^{\mathbf{WT}}$
940 transcriptomes to a high-resolution reference data set (42). Spearman rank coefficients (ρ)
941 describe the correlation between the sampled transcriptomes and the reference data set. The
942 time points with the highest correlation coefficient are indicated. **(D)** Principal component
943 analysis (PCA) of RNA-Seq data by condition and time point (TP). The outlier at TP3
944 (highlighted by an arrow) was removed from the analysis. **(E)** PCA of RNA-Seq data by
945 condition and time point without the TP3 outlier mentioned in (D). Exclusion of this sample
946 did not affect the overall pattern.

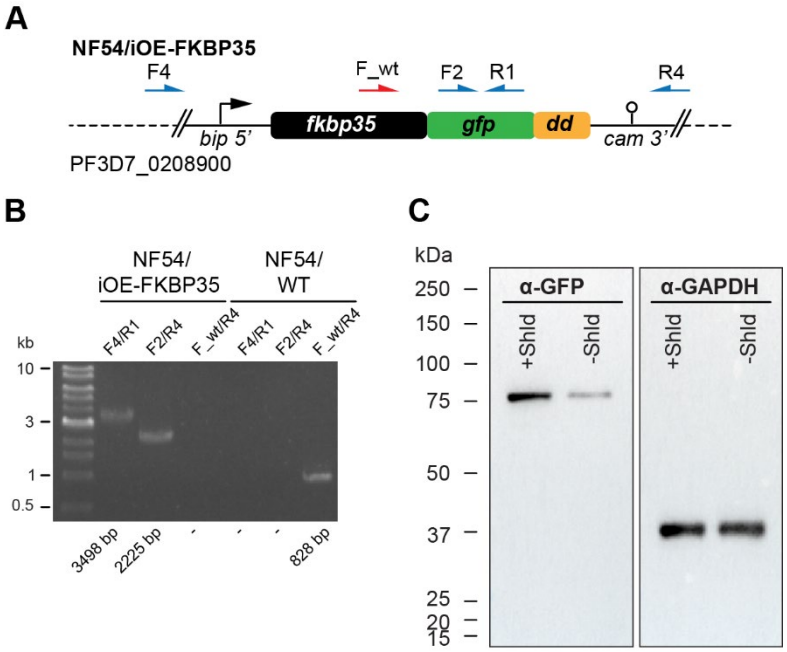

Figure S4. Characterization of NF54/iOE-FKBP35 parasites.

(A) Schematic of the modified *p230p* locus (PF3D7_0208900) in NF54/iOE-FKBP35 parasites, in which the overexpression cassette was introduced. This cassette consists of a *bip* promoter upstream of coding sequences of *fkbp35*, green fluorescent protein (*gfp*) and destabilization domain (*dd*), followed by the *cam 3'* region. Names and binding sites of the primers used for diagnostic PCRs are indicated. The primer F_wt only binds the unmodified *p230p* sequence. **(B)** Diagnostic PCRs performed on gDNA of NF54/iOE-FKBP35 parasites to confirm correct editing of the locus. PCRs performed on NF54/WT gDNA served as control. Numbers at the bottom indicate the expected band sizes. **(C)** Expression levels of the FKBP35-GFP-DD fusion protein were assessed by Western blot. Parasite cultures were split at 0-6 hpi and treated with Shield or the vehicle control EtOH. Protein lysates were collected 40 h later. α-GAPDH served as loading control. The expected size of the FKBP35-GFP-DD fusion protein is 74.2 kDa.

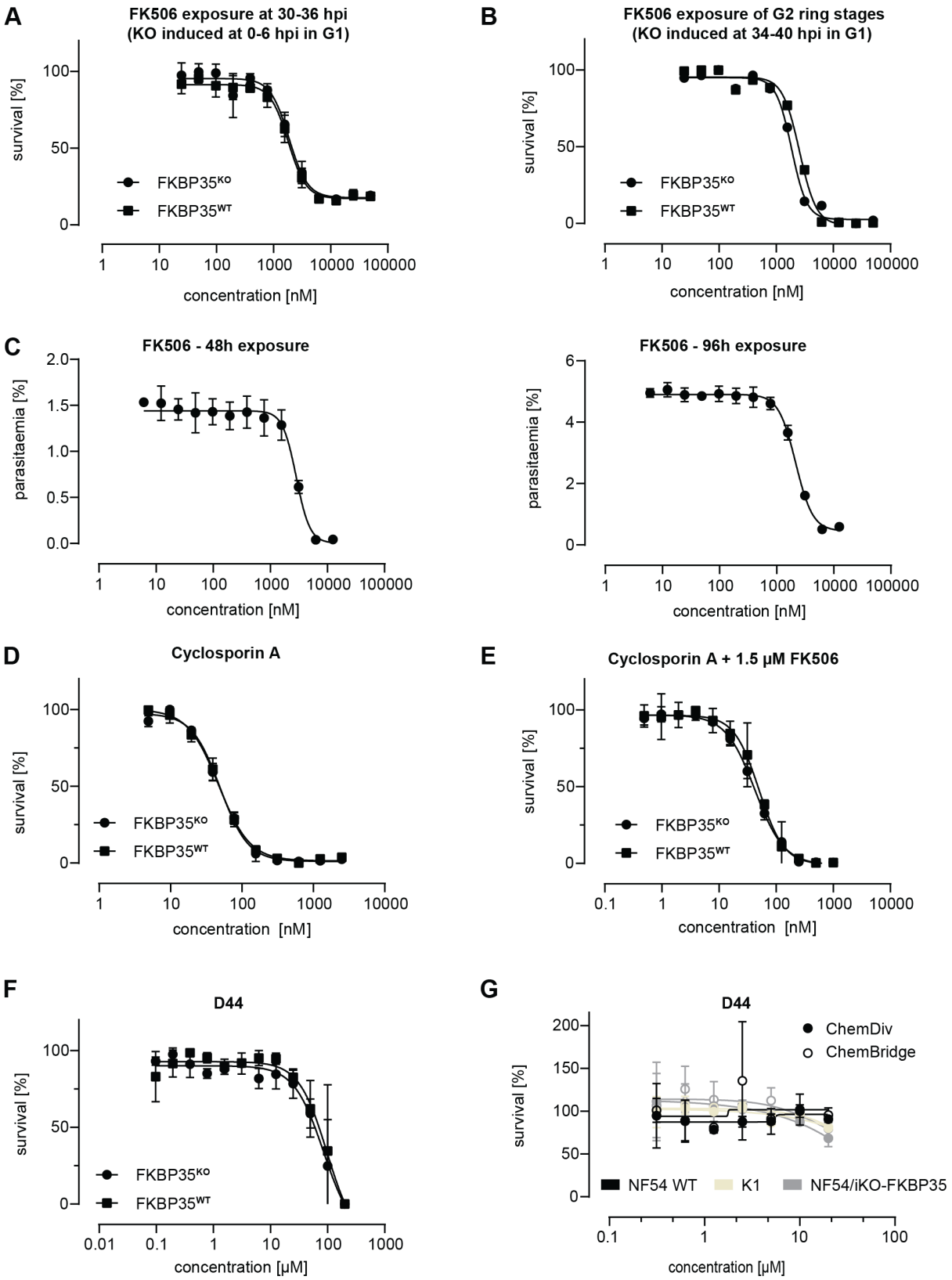

Figure S5. FKBP-targeting drugs fail at inhibiting parasite *Pf*FKBP35.

(A) Dose-response effect of FK506 on FKBP35^{KO} and FKBP35^{WT} parasites. The knockout was induced at 0-6 hpi and parasites were exposed to FK506 at 30-36 hpi. Survival rates were measured by flow cytometry in G2. n=3, error bars represent the standard error of the mean.

965 **(B)** Dose-response effect of FK506 on FKBP35^{KO} and FKBP35^{WT} parasites. The knockout was
966 induced at 34-40 hpi in G1. Ring stage parasites of G2 were exposed to FK506 for 48 hours
967 and survival rates were measured by flow cytometry in G3. Data points represent survival rates
968 measured in a single experiment performed in technical duplicates. **(C)** Dose-response effect of
969 FK506 on FKBP35^{WT} parasites over two IDCs. Parasites at 0-6 hpi were exposed to FK506 and
970 incubated for 96 hours. Parasitaemia was measured by flow cytometry after 48 hours and 96
971 hours. Medium containing the appropriate drug concentrations was changed after 48 hours. n=3,
972 error bars represent the standard error of the mean. **(D)** Dose-response effect of cyclosporin A
973 on FKBP35^{KO} and FKBP35^{WT} parasites. Cylocsporin A, a known inhibitor of calcineurin when
974 complexed with FKBP in other organisms (79), did not alter drug susceptibility between
975 FKBP35^{KO} and FKBP35^{WT} parasites, suggesting that *Pf*FKBP35 is not involved in regulating
976 calcineurin activity. The knockout was induced at 0-6 hpi. Parasites were exposed to
977 cyclosporin A for 48 hours. n=3, error bars represent the standard error of the mean. **(E)** Dose-
978 response effect of cyclosporin A in combination with a constant FK506 concentration on
979 FKBP35^{KO} and FKBP35^{WT} parasites. The knockout was induced at 0-6 hpi. Parasites were
980 subsequently exposed to cyclosporin A and 1.5 µM FK506 for 48 h. n=3, error bars represent
981 the standard error of the mean. **(F)** Dose-response effect of D44 on FKBP35^{KO} and FKBP35^{WT}.
982 The knockout was induced at 0-6 hpi and parasites were exposed to D44 for 48 hours thereafter.
983 Survival rates were determined using flow cytometry. n=3, error bars represent the standard
984 error of the mean. **(G)** Dose-response effect of D44 on NF54 WT, K1 and NF54/iKO-FKBP35
985 parasites after 72 h exposure. Survival rates were determined using a hypoxanthine
986 incorporation assay. Data points represent the mean of two technical replicates. Error bars
987 represent the standard error of the mean.

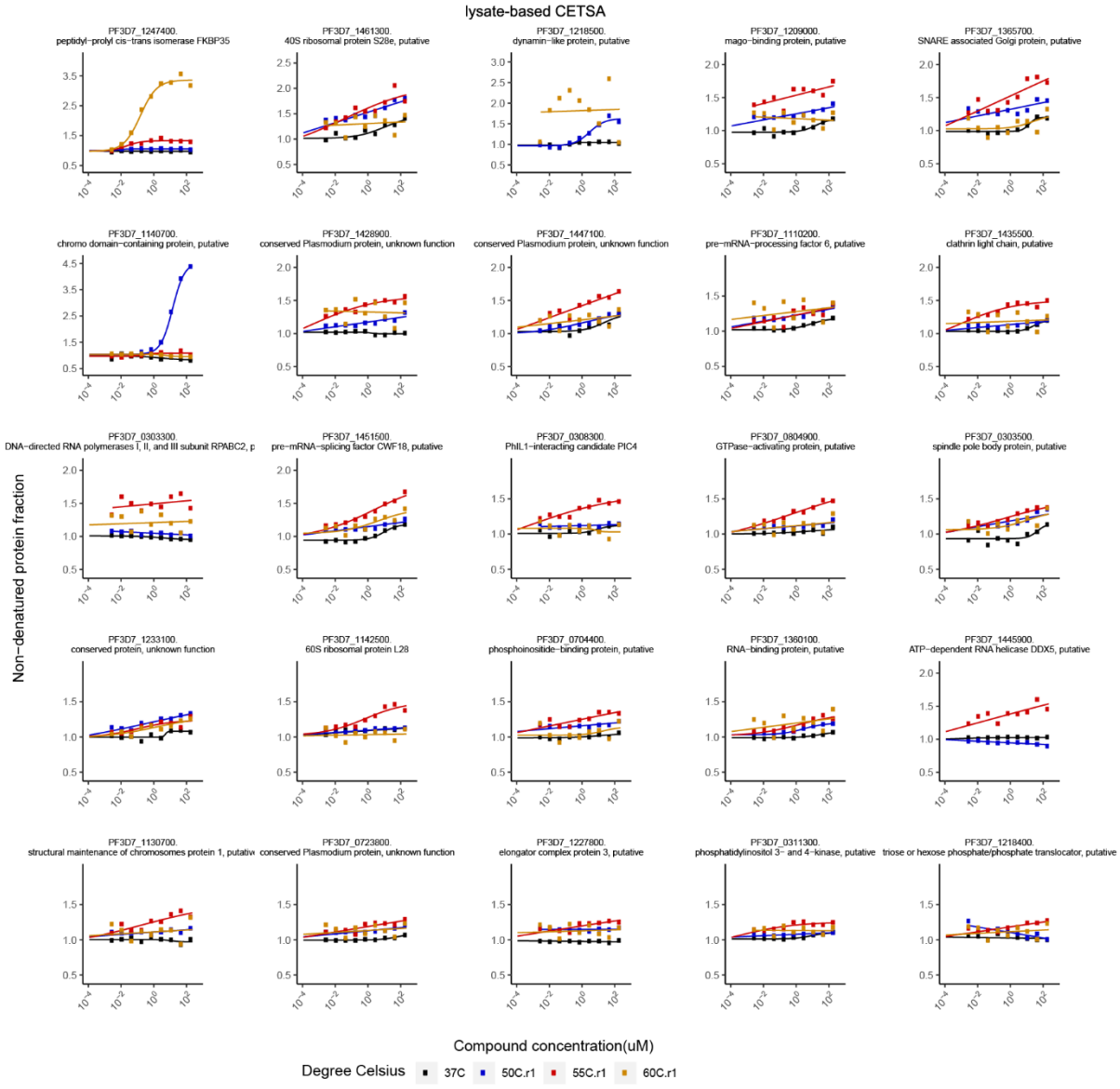

Figure S6. Putative FK506 interaction partners identified by protein lysate-based CETSA.

Proteins with an area under the curve (ΔAUC in protein lysate-based CETSA) greater than two median absolute deviations and an R^2 greater than 0.8 are listed. Bullets represent the abundance of non-denatured proteins in response to increasing FK506 concentrations under thermal challenge relative to a DMSO control. Colors indicate the temperatures used for protein denaturation; the black curve represents the non-denaturing control.

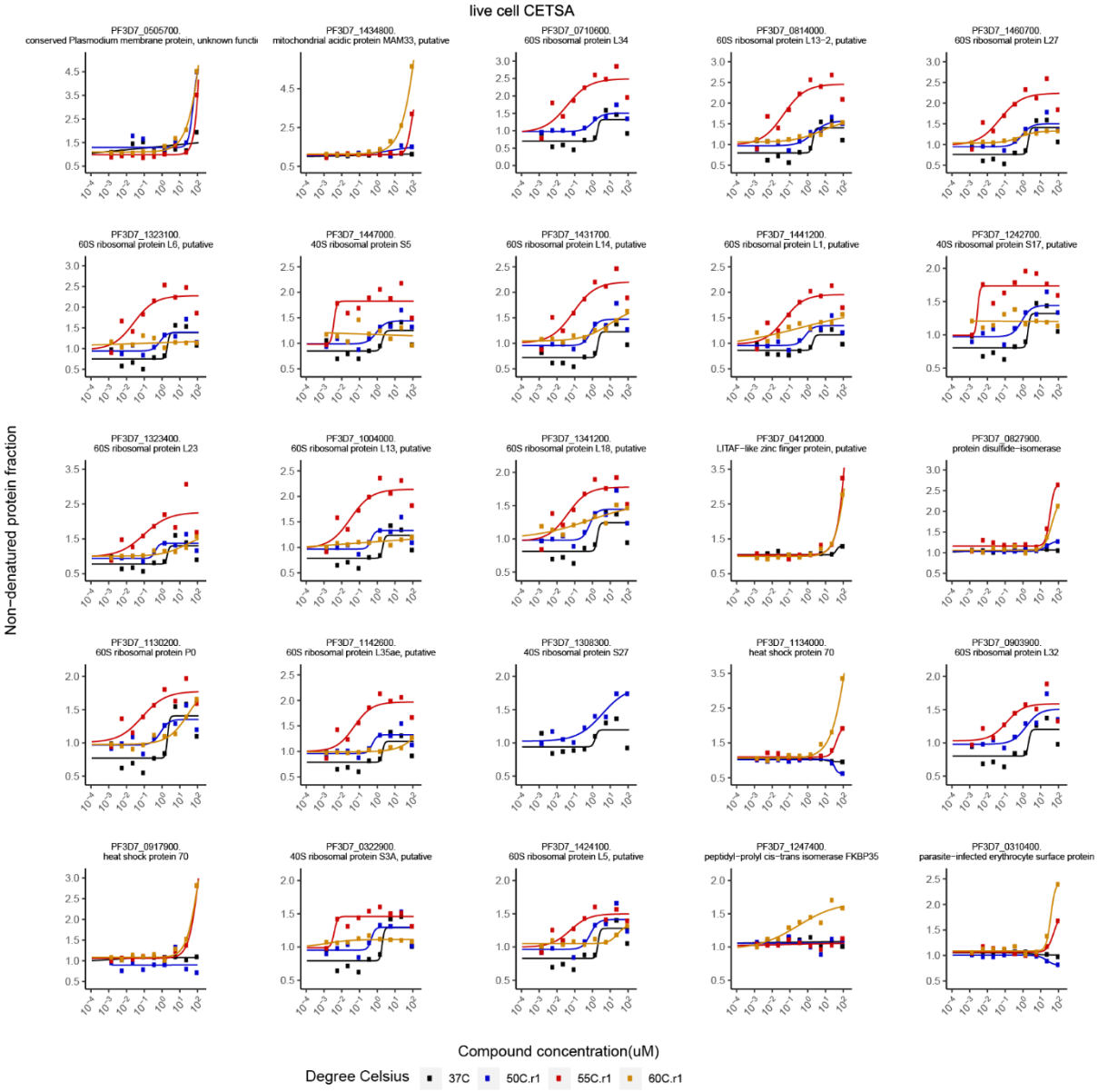

Figure S7. Putative FK506 interaction partners identified by live cell CETSA.

Proteins with an area under the curve (ΔAUC in live cell CETSA) greater than two median absolute deviations and an R^2 greater than 0.8 are listed. Bullets represent the abundance of non-denatured proteins in response to increasing FK506 concentrations under thermal challenge relative to a DMSO control. Colors indicate the temperatures used for heat challenge; the black curve represents the non-denaturing control.

1003 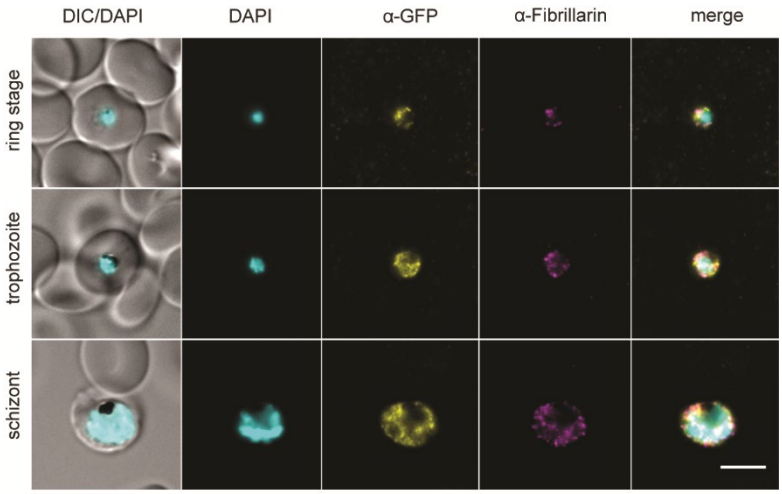

1004 **Figure S8. *Pf*FKBP35 localizes near fibrillarin-dense nuclear regions.**

1005 Localization of *Pf*FKBP35 (GFP) and fibrillarin in NF54/iKD-FKBP35 parasites at the ring,
1006 trophozoite and schizont stage assessed by immunofluorescence. DNA was stained with DAPI.
1007 Representative images are shown. Scale bar: 5 µm. DIC, differential interference contrast.

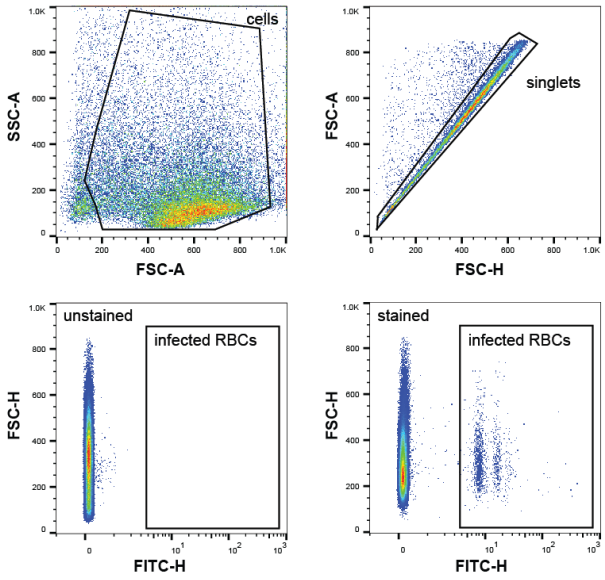

Figure S9. Gating strategy of flow cytometry data.

Representative flow cytometry plots of formaldehyde/glutaraldehyde-fixed parasite cultures are shown. The first plot shows the gate to distinguish cells from small debris (SSC-A vs. FSC-A). The 'singlets' gate (FSC-A vs. FSC-H) removes events with more than one cells. SYBR Green fluorescence intensity is used to identify parasite-infected RBCs (FSC-H vs. FITC-H). SSC, side scatter. FSC, forward scatter. FITC, fluorescein-5-isothiocyanate. A, area. H, height.

1015 **Table S1.** Mass spectrometry data comparing the proteomes of FKBP35^{KO} and FKBP35^{WT}
1016 parasites.

1017 **Table S2.** RNA-seq data comparing the transcriptomes of FKBP35^{KO} and FKBP35^{WT}
1018 parasites.

1019 **Table S3.** CETSA data showing the relative abundance of soluble proteins under non-
1020 denaturing and denaturing conditions in response to increasing FK506 concentrations.

1021 **Table S4.** Oligonucleotides used in this study.

1022

1023 # 5 References

1024 1. WHO. World malaria report 2022. Geneva: WHO; 2022.

1025 2. Ippolito MM, Moser KA, Kabuya JB, Cunningham C, Juliano JJ. Antimalarial Drug
1026 Resistance and Implications for the WHO Global Technical Strategy. Curr Epidemiol Rep.
1027 2021;8(2):46-62.

1028 3. Bell A, Wernli B, Franklin RM. Roles of peptidyl-prolyl cis-trans isomerase and
1029 calcineurin in the mechanisms of antimalarial action of cyclosporin A, FK506, and rapamycin.
1030 Biochem Pharmacol. 1994;48(3):495-503.

1031 4. Bharatham N, Chang MW, Yoon HS. Targeting FK506 binding proteins to fight
1032 malarial and bacterial infections: current advances and future perspectives. Curr Med Chem.
1033 2011;18(12):1874-89.

1034 5. Monaghan P, Bell A. A Plasmodium falciparum FK506-binding protein (FKBP) with
1035 peptidyl-prolyl cis-trans isomerase and chaperone activities. Mol Biochem Parasitol.
1036 2005;139(2):185-95.

1037 6. Bell A, Monaghan P, Page AP. Peptidyl-prolyl cis-trans isomerases (immunophilins)
1038 and their roles in parasite biochemistry, host-parasite interaction and antiparasitic drug
1039 action. Int J Parasitol. 2006;36(3):261-76.

1040 7. Kolos JM, Voll AM, Bauder M, Hausch F. FKBP Ligands-Where We Are and Where to
1041 Go? Front Pharmacol. 2018;9:1425.

1042 8. Kang CB, Hong Y, Dhe-Paganon S, Yoon HS. FKBP family proteins: immunophilins
1043 with versatile biological functions. Neurosignals. 2008;16(4):318-25.

1044 9. Bose S, Weikl T, Bügl H, Buchner J. Chaperone function of Hsp90-associated
1045 proteins. Science. 1996;274(5293):1715-7.

1046 10. Furutani M, Ideno A, Iida T, Maruyama T. FK506 binding protein from a thermophilic
1047 archaeon, methanococcus thermolithotrophicus, has chaperone-like activity in vitro.
1048 Biochemistry. 2000;39(10):2822.

1049 11. Yang WM, Yao YL, Seto E. The FK506-binding protein 25 functionally associates with
1050 histone deacetylases and with transcription factor YY1. Embo j. 2001;20(17):4814-25.

1051 12. Kasahara K, Nakayama R, Shiwa Y, Kanesaki Y, Ishige T, Yoshikawa H, et al. Fpr1,
1052 a primary target of rapamycin, functions as a transcription factor for ribosomal protein
1053 genes cooperatively with Hmo1 in Saccharomyces cerevisiae. PLoS Genet.
1054 2020;16(6):e1008865.

1055 13. Cardenas ME, Zhu D, Heitman J. Molecular mechanisms of immunosuppression by
1056 cyclosporine, FK506, and rapamycin. Curr Opin Nephrol Hypertens. 1995;4(6):472-7.

1057 14. Leneghan D, Bell A. Immunophilin-protein interactions in Plasmodium falciparum.
1058 Parasitology. 2015;142(11):1404-14.

1059 15. Yoon HR, Kang CB, Chia J, Tang K, Yoon HS. Expression, purification, and
1060 molecular characterization of Plasmodium falciparum FK506-binding protein 35 (PfFKBP35).
1061 Protein Expr Purif. 2007;53(1):179-85.

1062 16. Kumar R, Adams B, Musiyenko A, Shulyayeva O, Barik S. The FK506-binding protein
1063 of the malaria parasite, Plasmodium falciparum, is a FK506-sensitive chaperone with FK506-
1064 independent calcineurin-inhibitory activity. Mol Biochem Parasitol. 2005;141(2):163-73.

1065 17. Alag R, Bharatham N, Dong A, Hills T, Harikishore A, Widjaja AA, et al.
1066 Crystallographic structure of the tetratricopeptide repeat domain of Plasmodium falciparum
1067 FKBP35 and its molecular interaction with Hsp90 C-terminal pentapeptide. Protein Sci.
1068 2009;18(10):2115-24.

1069 18. Zhang M, Wang C, Otto TD, Oberstaller J, Liao X, Adapa SR, et al. Uncovering the
1070 essential genes of the human malaria parasite Plasmodium falciparum by saturation
1071 mutagenesis. Science. 2018;360(6388).

1072 19. Alag R, Qureshi IA, Bharatham N, Shin J, Lescar J, Yoon HS. NMR and
1073 crystallographic structures of the FK506 binding domain of human malarial parasite
1074 Plasmodium vivax FKBP35. Protein Sci. 2010;19(8):1577-86.

1075 20. Goh CKW, Silvester J, Wan Mahadi WNS, Chin LP, Ying LT, Leow TC, et al.
1076 Expression and characterization of functional domains of FK506-binding protein 35 from
1077 Plasmodium knowlesi. Protein Eng Des Sel. 2018;31(12):489-98.

1078 21. Bianchin A, Allemand F, Bell A, Chubb AJ, Guichou JF. Two crystal structures of the
1079 FK506-binding domain of Plasmodium falciparum FKBP35 in complex with rapamycin at high
1080 resolution. Acta Crystallogr D Biol Crystallogr. 2015;71(Pt 6):1319-27.

1081 22. Kotaka M, Ye H, Alag R, Hu G, Bozdech Z, Preiser PR, et al. Crystal structure of the
1082 FK506 binding domain of Plasmodium falciparum FKBP35 in complex with FK506.
1083 Biochemistry. 2008;47(22):5951-61.

1084 23. MacDonald CA, Boyd RJ. Computational insights into the suicide inhibition of
1085 Plasmodium falciparum Fk506-binding protein 35. Bioorg Med Chem Lett. 2015;25(16):3221-
1086 5.

1087 24. Harikishore A, Niang M, Rajan S, Preiser PR, Yoon HS. Small molecule Plasmodium
1088 FKBP35 inhibitor as a potential antimalaria agent. Sci Rep. 2013;3:2501.

1089 25. Harikishore A, Leow ML, Niang M, Rajan S, Pasunooti KK, Preiser PR, et al.
1090 Adamantyl derivative as a potent inhibitor of Plasmodium FK506 binding protein 35. ACS
1091 Med Chem Lett. 2013;4(11):1097-101.

1092 26. Rajan S, Yoon HS. Structural insights into Plasmodium PPIases. Front Cell Infect
1093 Microbiol. 2022;12:931635.

1094 27. MacDonald CA, Boyd RJ. Molecular docking study of macrocycles as Fk506-binding
1095 protein inhibitors. J Mol Graph Model. 2015;59:117-22.

1096 28. Deepa P, Thirumeignanam D. Understanding the potency of malarial ligand (D44) in
1097 plasmodium FKBP35 and modelled halogen atom (Br, Cl, F) functional groups. J Mol Graph
1098 Model. 2020;97:107553.

1099 29. Atack TC, Raymond DD, Blomquist CA, Pasaje CF, McCarren PR, Moroco J, et al.
1100 Targeted Covalent Inhibition of Plasmodium FK506 Binding Protein 35. ACS Med Chem Lett.
1101 2020;11(11):2131-8.

1102 30. Armstrong CM, Goldberg DE. An FKBP destabilization domain modulates protein
1103 levels in Plasmodium falciparum. Nat Methods. 2007;4(12):1007-9.

1104 31. Banaszynski LA, Chen LC, Maynard-Smith LA, Ooi AG, Wandless TJ. A rapid,
1105 reversible, and tunable method to regulate protein function in living cells using synthetic
1106 small molecules. Cell. 2006;126(5):995-1004.

1107 32. Collins CR, Das S, Wong EH, Andenmatten N, Stallmach R, Hackett F, et al. Robust
1108 inducible Cre recombinase activity in the human malaria parasite Plasmodium falciparum
1109 enables efficient gene deletion within a single asexual erythrocytic growth cycle. Mol
1110 Microbiol. 2013;88(4):687-701.

1111 33. Jones ML, Das S, Belda H, Collins CR, Blackman MJ, Treeck M. A versatile strategy
1112 for rapid conditional genome engineering using loxP sites in a small synthetic intron in
1113 Plasmodium falciparum. Sci Rep. 2016;6:21800.

1114 34. Kucharski M, Tripathi J, Nayak S, Zhu L, Wirjanata G, van der Pluijm RW, et al. A
1115 comprehensive RNA handling and transcriptomics guide for high-throughput processing of
1116 Plasmodium blood-stage samples. Malar J. 2020;19(1):363.

1117 35. Wiley JD, Merino EF, Krai PM, McLean KJ, Tripathi AK, Vega-Rodríguez J, et al.
1118 Isoprenoid precursor biosynthesis is the essential metabolic role of the apicoplast during
1119 gametocytogenesis in Plasmodium falciparum. Eukaryot Cell. 2015;14(2):128-39.

1120 36. Kennedy K, Cobbold SA, Hanssen E, Birnbaum J, Spillman NJ, McHugh E, et al.
1121 Delayed death in the malaria parasite Plasmodium falciparum is caused by disruption of
1122 prenylation-dependent intracellular trafficking. PLoS Biol. 2019;17(7):e3000376.

1123 37. Mi H, Ebert D, Muruganujan A, Mills C, Albou LP, Mushayamaha T, et al. PANTHER
1124 version 16: a revised family classification, tree-based classification tool, enhancer regions
1125 and extensive API. Nucleic Acids Res. 2021;49(D1):D394-d403.

1126 38. Boisvert FM, van Koningsbruggen S, Navascués J, Lamond AI. The multifunctional
1127 nucleolus. Nat Rev Mol Cell Biol. 2007;8(7):574-85.

1128 39. Nissan TA, Bassler J, Petfalski E, Tollervey D, Hurt E. 60S pre-ribosome formation
1129 viewed from assembly in the nucleolus until export to the cytoplasm. Embo j.
1130 2002;21(20):5539-47.

1131 40. Plouffe D, Brinker A, McNamara C, Henson K, Kato N, Kuhen K, et al. In silico activity
1132 profiling reveals the mechanism of action of antimalarials discovered in a high-throughput
1133 screen. Proc Natl Acad Sci U S A. 2008;105(26):9059-64.

1134 41. Schmidt EK, Clavarino G, Ceppi M, Pierre P. SUnSET, a nonradioactive method to
1135 monitor protein synthesis. Nat Methods. 2009;6(4):275-7.

1136 42. Bozdech Z, Llinás M, Pulliam BL, Wong ED, Zhu J, DeRisi JL. The transcriptome of
1137 the intraerythrocytic developmental cycle of Plasmodium falciparum. PLoS Biol.
1138 2003;1(1):E5.

1139 43. Barnum KJ, O'Connell MJ. Cell cycle regulation by checkpoints. Methods Mol Biol.
1140 2014;1170:29-40.

1141 44. Monaghan P, Leneghan DB, Shaw W, Bell A. The antimalarial action of FK506 and
1142 rapamycin: evidence for a direct effect on FK506-binding protein PfFKBP35. Parasitology.
1143 2017;144(7):869-76.

1144 45. Van Duyne GD, Standaert RF, Karplus PA, Schreiber SL, Clardy J. Atomic structure
1145 of FKBP-FK506, an immunophilin-immunosuppressant complex. Science.
1146 1991;252(5007):839-42.

1147 46. Dziekan JM, Yu H, Chen D, Dai L, Wirjanata G, Larsson A, et al. Identifying purine
1148 nucleoside phosphorylase as the target of quinine using cellular thermal shift assay. Sci
1149 Transl Med. 2019;11(473).

1150 47. Dziekan JM, Wirjanata G, Dai L, Go KD, Yu H, Lim YT, et al. Cellular thermal shift
1151 assay for the identification of drug-target interactions in the Plasmodium falciparum
1152 proteome. Nat Protoc. 2020;15(6):1881-921.

1153 48. Tan CSH, Go KD, Bisteau X, Dai L, Yong CH, Prabhu N, et al. Thermal proximity
1154 coaggregation for system-wide profiling of protein complex dynamics in cells. Science.
1155 2018;359(6380):1170-7.

1156 49. Paul AS, Saha S, Engelberg K, Jiang RH, Coleman BI, Kosber AL, et al. Parasite
1157 Calcineurin Regulates Host Cell Recognition and Attachment by Apicomplexans. Cell Host
1158 Microbe. 2015;18(1):49-60.

1159 50. Desjardins RE, Canfield CJ, Haynes JD, Chulay JD. Quantitative assessment of
1160 antimalarial activity in vitro by a semiautomated microdilution technique. Antimicrob Agents
1161 Chemother. 1979;16(6):710-8.

1162 51. Ünal CM, Steinert M. FKBPs in bacterial infections. Biochim Biophys Acta.
1163 2015;1850(10):2096-102.

1164 52. Gudavicius G, Dilworth D, Serpa JJ, Sessler N, Petrotchenko EV, Borchers CH, et al.
1165 The prolyl isomerase, FKBP25, interacts with RNA-engaged nucleolin and the pre-60S
1166 ribosomal subunit. Rna. 2014;20(7):1014-22.

1167 53. Sydorskyy Y, Dilworth DJ, Halloran B, Yi EC, Makhnevych T, Wozniak RW, et al.
1168 Nop53p is a novel nucleolar 60S ribosomal subunit biogenesis protein. Biochem J.
1169 2005;388(Pt 3):819-26.

1170 54. Ferbitz L, Maier T, Patzelt H, Bukau B, Deuerling E, Ban N. Trigger factor in complex
1171 with the ribosome forms a molecular cradle for nascent proteins. Nature.
1172 2004;431(7008):590-6.

1173 55. Callebaut I, Mornon JP. Trigger factor, one of the Escherichia coli chaperone
1174 proteins, is an original member of the FKBP family. FEBS Lett. 1995;374(2):211-5.

1175 56. Rodriguez-Corona U, Sobol M, Rodriguez-Zapata LC, Hozak P, Castano E. Fibrillarin
1176 from Archaea to human. Biol Cell. 2015;107(6):159-74.

1177 57. Thiry M, Lafontaine DL. Birth of a nucleolus: the evolution of nucleolar compartments.
1178 Trends in cell biology. 2005;15(4):194-9.

1179 58. Lambros C, Vanderberg JP. Synchronization of Plasmodium falciparum erythrocytic
1180 stages in culture. J Parasitol. 1979;65(3):418-20.

1181 59. Trager W, Jenson JB. Cultivation of malarial parasites. Nature. 1978;273(5664):621-
1182 2.

1183 60. Brancucci NMB, Gerdt JP, Wang C, De Niz M, Philip N, Adapa SR, et al.
1184 Lysophosphatidylcholine Regulates Sexual Stage Differentiation in the Human Malaria
1185 Parasite Plasmodium falciparum. Cell. 2017;171(7):1532-44.e15.

1186 61. Filarsky M, Fraschka SA, Niederwieser I, Brancucci NMB, Carrington E, Carrió E, et
1187 al. GDV1 induces sexual commitment of malaria parasites by antagonizing HP1-dependent
1188 gene silencing. Science. 2018;359(6381):1259-63.

1189 62. Knuepfer E, Napiorkowska M, van Ooij C, Holder AA. Generating conditional gene
1190 knockouts in Plasmodium - a toolkit to produce stable DiCre recombinase-expressing
1191 parasite lines using CRISPR/Cas9. Sci Rep. 2017;7(1):3881.

1192 63. Gibson DG, Young L, Chuang RY, Venter JC, Hutchison CA, 3rd, Smith HO.
1193 Enzymatic assembly of DNA molecules up to several hundred kilobases. Nat Methods.
1194 2009;6(5):343-5.

1195 64. Ashdown GW, Dimon M, Fan M, Sánchez-Román Terán F, Witmer K, Gaboriau DCA,
1196 et al. A machine learning approach to define antimalarial drug action from heterogeneous
1197 cell-based screens. Sci Adv. 2020;6(39).

1198 65. Tibúrcio M, Yang ASP, Yahata K, Suárez-Cortés P, Belda H, Baumgarten S, et al. A
1199 Novel Tool for the Generation of Conditional Knockouts To Study Gene Function across the
1200 Plasmodium falciparum Life Cycle. mBio. 2019;10(5).

1201 66. Thommen BT, Passecker A, Buser T, Hitz E, Voss TS, Brancucci NMB. Revisiting the
1202 Effect of Pharmaceuticals on Transmission Stage Formation in the Malaria Parasite
1203 Plasmodium falciparum. Front Cell Infect Microbiol. 2022;12:802341.

1204 67. Thomas JA, Collins CR, Das S, Hackett F, Graindorge A, Bell D, et al. Development
1205 and Application of a Simple Plaque Assay for the Human Malaria Parasite Plasmodium
1206 falciparum. PLoS One. 2016;11(6):e0157873.

1207 68. Daubenberger CA, Tisdale EJ, Curcic M, Diaz D, Silvie O, Mazier D, et al. The N'-
1208 terminal domain of glyceraldehyde-3-phosphate dehydrogenase of the apicomplexan
1209 Plasmodium falciparum mediates GTPase Rab2-dependent recruitment to membranes. Biol
1210 Chem. 2003;384(8):1227-37.

1211 69. Ahrné E, Glatter T, Viganò C, Schubert C, Nigg EA, Schmidt A. Evaluation and
1212 Improvement of Quantification Accuracy in Isobaric Mass Tag-Based Protein Quantification
1213 Experiments. J Proteome Res. 2016;15(8):2537-47.

1214 70. Ritchie ME, Phipson B, Wu D, Hu Y, Law CW, Shi W, et al. limma powers differential
1215 expression analyses for RNA-sequencing and microarray studies. Nucleic Acids Res.
1216 2015;43(7):e47.

1217 71. McLean KJ, Jacobs-Lorena M. Plasmodium falciparum Maf1 Confers Survival upon
1218 Amino Acid Starvation. mBio. 2017;8(2).

1219 72. Kim D, Paggi JM, Park C, Bennett C, Salzberg SL. Graph-based genome alignment
1220 and genotyping with HISAT2 and HISAT-genotype. Nat Biotechnol. 2019;37(8):907-15.

1221 73. Aurrecoechea C, Brestelli J, Brunk BP, Dommer J, Fischer S, Gajria B, et al.
1222 PlasmoDB: a functional genomic database for malaria parasites. Nucleic Acids Res.
1223 2009;37(Database issue):D539-43.

1224 74. Love MI, Huber W, Anders S. Moderated estimation of fold change and dispersion for
1225 RNA-seq data with DESeq2. Genome Biol. 2014;15(12):550.

1226 75. Blighe K, Rana S, Lewis M. EnhancedVolcano: Publication-ready volcano plots with
1227 enhanced colouring and labeling. R package version 1.16.0.
1228 https://githubcom/kevinblighe/EnhancedVolcano. 2022.

1229 76. Kassambara A. ggcorrplot: Visualization of a Correlation Matrix using 'ggplot2'. R
1230 package version 0.1.3, . https://CRANR-projectorg/package=ggcorrplot. 2022.

1231 77. Yeh E, DeRisi JL. Chemical rescue of malaria parasites lacking an apicoplast defines
1232 organelle function in blood-stage Plasmodium falciparum. PLoS Biol. 2011;9(8):e1001138.

1233 78. Lu KY, Pasaje CFA, Srivastava T, Loiselle DR, Niles JC, Derbyshire E.
1234 Phosphatidylinositol 3-phosphate and Hsp70 protect Plasmodium falciparum from heat-
1235 induced cell death. Elife. 2020;9.

1236 79. Dumont FJ. FK506, an immunosuppressant targeting calcineurin function. Curr Med
1237 Chem. 2000;7(7):731-48.

1238